A Comparison of Two Vertical-Mixing Schemes in a Pacific Ocean General Circulation Model

XIANJIN LI AND YI CHAO

Jet Propulsion Laboratory, California Institute of Technology, Pasadena, California

JAMES C. MCWILLIAMS

University of California, Los Angeles, Los Angeles, California

LEE-LUENG FU

Jet Propulsion Laboratory, California Institute of Technology, Pasadena, California

(Manuscript received 17 May 1999, in final form 16 June 2000)

ABSTRACT

The upper Pacific Ocean Current and temperature have been simulated by a three-dimensional ocean general circulation model (OGCM) with two different vertical-mixing schemes. One corresponds to the modified Richardson number–dependent scheme of Pacanowski and Philander (PP); the other is adapted from the newly developed *K*-Profile Parameterization (KPP) scheme. The performance of both schemes in a Pacific OGCM is evaluated under the same model configuration and boundary conditions. Model and data comparisons are made for the mean state, annual cycle, and interannual-to-interdecadal variability. In the Tropics, both the PP and KPP schemes produce reasonably realistic tropical thermal and current structures; however, KPP is better than PP in several important aspects. For example, the KPP scheme simulates a more realistic thermocline and significantly reduces the cold surface temperature bias in the eastern equatorial Pacific. The depth of the maximum Equatorial Undercurrent simulated by the KPP scheme is much closer to the observation. In the extratropics the KPP scheme is significantly better than the PP scheme in simulating the thermal and current structures, including the annual mean, annual cycle, and interannual-to-interdecadal variability.

1. Introduction

It is well known that oceanic vertical mixing plays a prominent role in regulating the sea surface temperature (SST), a critical oceanic parameter in controlling the exchanges of energy and momentum between the ocean and atmosphere. Climate models with an aim to represent realistic ocean dynamics have to properly describe the vertical-mixing processes. The vertical mixing, because of the small-scale turbulent processes involved, usually cannot be explicitly resolved in ocean general circulation models (OGCMs) and has to be parameterized.

The conventional parameterization of the vertical mixing is to use an eddy diffusion model (the so-called *K* theory), which assumes a local relationship between eddy fluxes and model prognostic variables. The simplest example is to use a constant mixing coefficient everywhere (Bryan and Lewis 1979; Sarmiento and Bryan 1982). Although the constant mixing coefficient can be optimized for some specific regions, its application to models of basin to global scales is often problematic. One alternative is to relate the mixing coefficients to the local Richardson number (Ri) based on stability theory (Robinson 1966). The Ri number–dependent mixing scheme was demonstrated to have a reasonable skill in simulating the tropical circulation in three-dimensional OGCMs (Pacanowski and Philander 1981, hereafter as PP; Philander et al. 1987). Simulations with the PP scheme provide a good representation of the shear instability process in the tropical oceans. Therefore, they are significantly better in the Tropics than those with constant mixing coefficients. However, the PP scheme is still deficient in simulating several important aspects of the tropical circulation (Stockdale et al. 1993; Niiler et al. 1995). Comparison with turbulence measurements has shown that the PP scheme underestimates the turbulent mixing at low Ri, while overestimating the turbulence mixing at high Ri (Peters et al. 1988). As a result, the thermocline simulated by the PP scheme is much too diffused as compared to

Corresponding author address: Dr. X. Li, M/S 300-323, JPL, 4800 Oak Grove Drive, Pasadena, CA 91109-8099.
E-mail: Yi.Chao@jpl.nasa.gov

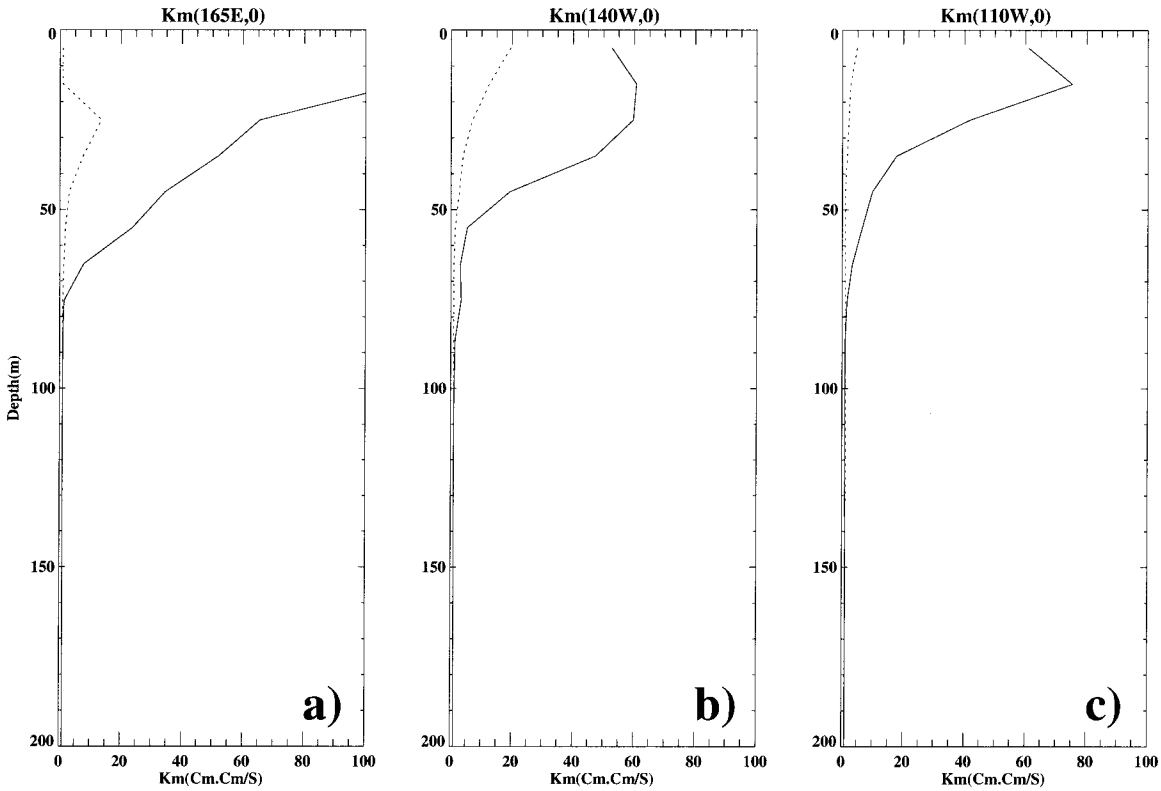

FIG. 1. The mean vertical profiles of K_m calculated from Eq. (13) in PP (dotted line) and Eq. (17) in KPP schemes (solid line) on the equator at (a) 165°E, (b) 140°W, and (c) 110°W, respectively. Unit is in $cm^2\ s^{-1}$.

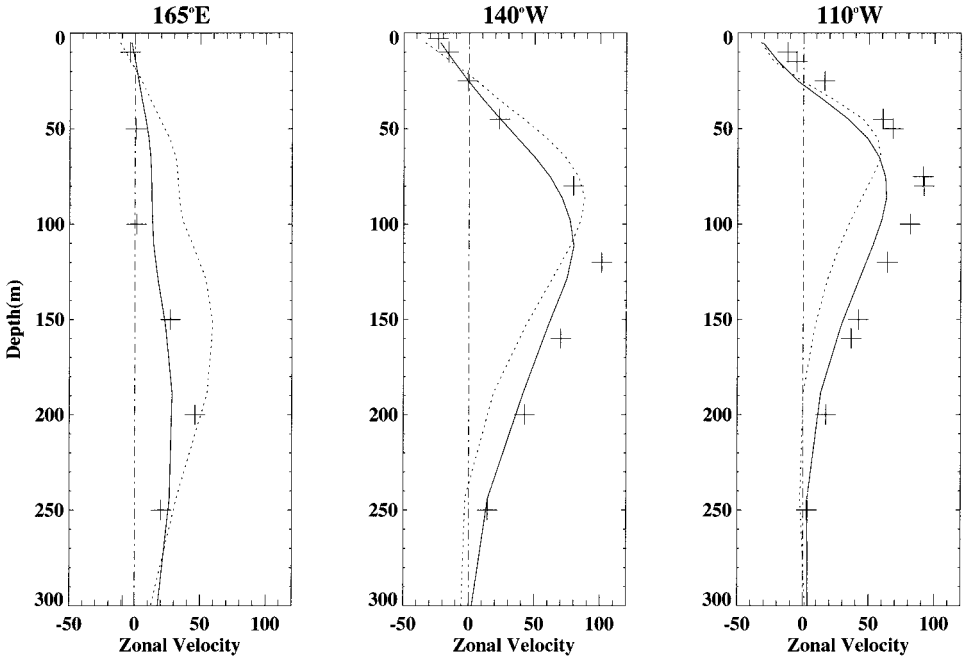

FIG. 2. The vertical profiles of long-term mean zonal current from the Tropical Ocean and Global Atmosphere (+), KPP (solid lines), and PP (dotted lines) along the equator at 165°E, 140°W, and 110°W, respectively. Unit is in $cm\ s^{-1}$.

TABLE 1. Vertical grid size and depth used in the NCOM.

Level	Grid size (m)	Depth (m)
1	10.00	10.00
2	10.00	20.00
3	10.00	30.00
4	10.00	40.00
5	10.00	50.00
6	10.05	60.05
7	10.17	70.22
8	10.44	80.66
9	11.05	91.71
10	12.33	104.04
11	14.87	118.91
12	19.70	138.61
13	28.38	166.99
14	43.20	210.19
15	67.18	277.37
16	103.92	381.29
17	157.13	538.42
18	229.85	768.27
19	323.33	1091.60
20	436.10	1527.70
21	562.20	2089.90
22	693.30	2783.20
23	816.10	3599.30
24	917.00	4516.30
25	983.70	5500.00

TABLE 2. Ekman spiral depth against vertical viscosity (lat 35°N).

D_E:m	K_m:cm^2 s^{-1}
4.86	1
15.38	10
21.75	20
26.64	30
30.76	40
34.40	50
48.64	100
108.77	500
153.82	1000

observations. The surface current simulated by the PP scheme is too strong, while the equatorial undercurrent is too shallow due to insufficient momentum penetration in the surface boundary layer (Niiler et al. 1995; Halpern et al. 1995). Furthermore, the performance of the PP scheme in the extratropics is rather poor (Stammer et al. 1996) due to the lack of explicit specification of other turbulence mixing processes (e.g., wind stirring and convective overturning).

One alternative is to use higher-order turbulence closure schemes; for example, the second-order closure scheme of level-1.5 (Blanke and Delecluse 1993), level-2.5 (Mellor and Yamada 1982; Rosati and Miyakoda 1988), or a modified second-order closure mixed layer scheme (Kantha and Clayson 1994). However, most of these higher-order closure schemes require high vertical resolution and/or high-frequency forcings and are, therefore, computationally costly for climate studies. These turbulence closure schemes attempt to parameterize small-scale motions with local prognostic variables in the model such as turbulence length scales, which are small in comparison to the boundary layer. Gnanadesikan and Weller (1995) and McWilliams et al. (1997) have argued that such schemes are unstable to large eddies, such as those in the Langmuir circulation. Meanwhile, the lack of explicit nonlocal turbulence transport in these turbulence closure schemes strongly limits their representation of the subgrid-scale mixing processes due to the difficulty in reproducing the entrainment flux at the bottom of the boundary layer (Ayotte et al. 1996).

Another alternative is to employ a vertically homogeneous mixed layer model (e.g., Kraus and Turner 1967; Garwood 1977) to simulate the near-surface processes. Using a layered model, Chen et al. (1994) recently developed a hybrid scheme by combining a homogeneous mixed layer model with Price's (Price et al. 1986) dynamical instability model. However, the coupling of such a bulk mixed layer model to a discrete level model is far from straightforward (Haidvogel and Beckmann 1999).

Recently a nonlocal vertical-mixing scheme called *K*-Profile Parameterization (KPP) has been proposed (Large et al. 1994). The KPP scheme does not assume a priori that the boundary layer is well mixed and explicitly predicts an ocean boundary layer depth. Within this boundary layer, the turbulent mixing is parameterized using a nonlocal bulk Richardson number and the similarity theory of turbulence. Below the boundary layer, the vertical mixing is parameterized through the local gradient Richardson number and a background mixing similar to the PP scheme.

The KPP formulation and its performance in one-dimensional models have been described in Large et al. (1994) and Large and Gent (1999). The annual-mean climatology from a three-dimensional coarse-resolution global ocean model with the KPP scheme can be found in Large et al. (1997), where numerical experiments are designed for comparsion with a baseline experiment with constant vertical-mixing coefficients.

What is the performance of the KPP scheme in a higher-resolution ocean general circulation model? Besides the annual-mean climatology, what kind of systematic impact does the KPP scheme have on simulating the important annual cycle and interannual-to-interdecadal variability? How significant are those improvements of the KPP scheme, if any, in simulating the thermal and current structures when compared with those conventional schemes? This paper describes the performance of the KPP scheme in simulating the three-dimensional thermal and current structures in a Pacific OGCM with enhanced resolutions in the Tropics. Systematic comparisons are made between the KPP and PP schemes in terms of the annual-mean climatology, annual cycle, and interannual-to-interdecadal variability. The description of the ocean model and model experiments is given in section 2. In section 3, both mixing schemes are described briefly. In section 4, the comparisons between the simulations and available obser-

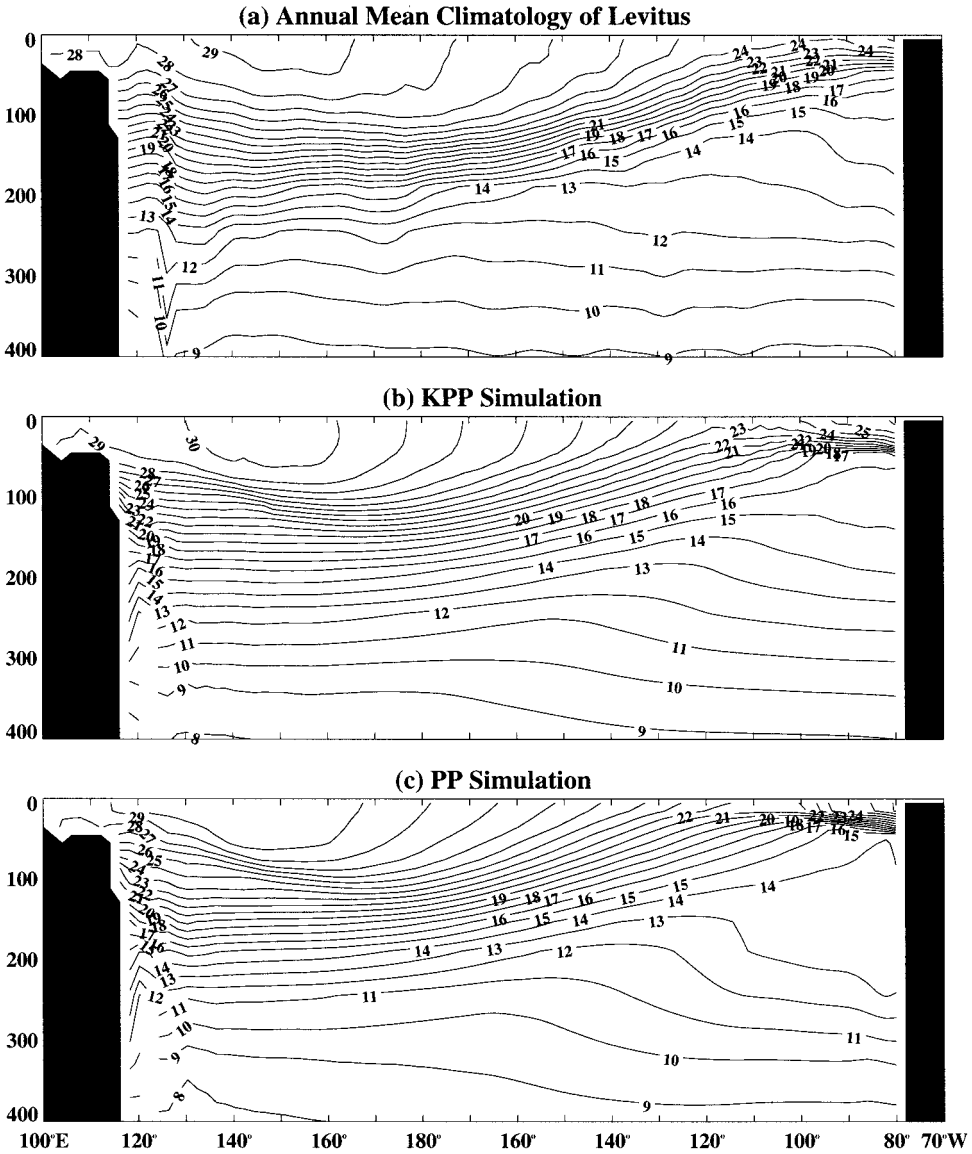

FIG. 3. Annual-mean temperature along the equator from (a) Levitus climatology, (b) KPP simulation, (c) PP simulation, and the difference between Levitus climatology and (d) KPP and (e) PP simulations. Unit is in °C.

vations are made. Finally, discussion and summary are presented in section 5.

2. Model description and experiment design

a. The model

The numerical model used in this study is based upon the National Center for Atmospheric Research's (NCAR) Climate System Modeling (CSM) Ocean Model (NCOM; Gent et al. 1998) that evolved from the version 1.0 of the Modular Ocean Model (Pacanowski et al. 1991) developed at the Geophysical Fluid Dynamical Laboratory. Among several new features implemented in NCOM, we want to emphasize the eddy-induced isopycnal transport parameterization (Gent and McWilliams 1990, hereinafter GM) and the KPP vertical-mixing scheme that will be explained in detail in section 3. The governing equations are the primitive equations in spherical coordinates, with hydrostatic, Boussinesq, and rigid-lid approximations (Bryan 1969; Cox 1984). The model domain covers the Pacific basin from 45°S to 65°N in latitude and from 100°E and 70°W in longitude. The longitudinal resolution is 2° uniformly. The latitudinal resolution is 0.5° within 10°S and 10°N and gradually increases poleward to 2° at and beyond 20°S and 20°N. There are 25 levels throughout the water column, with 5 uniform levels in the upper 50 m and 10 additional levels between 50 and 277 m (see Table

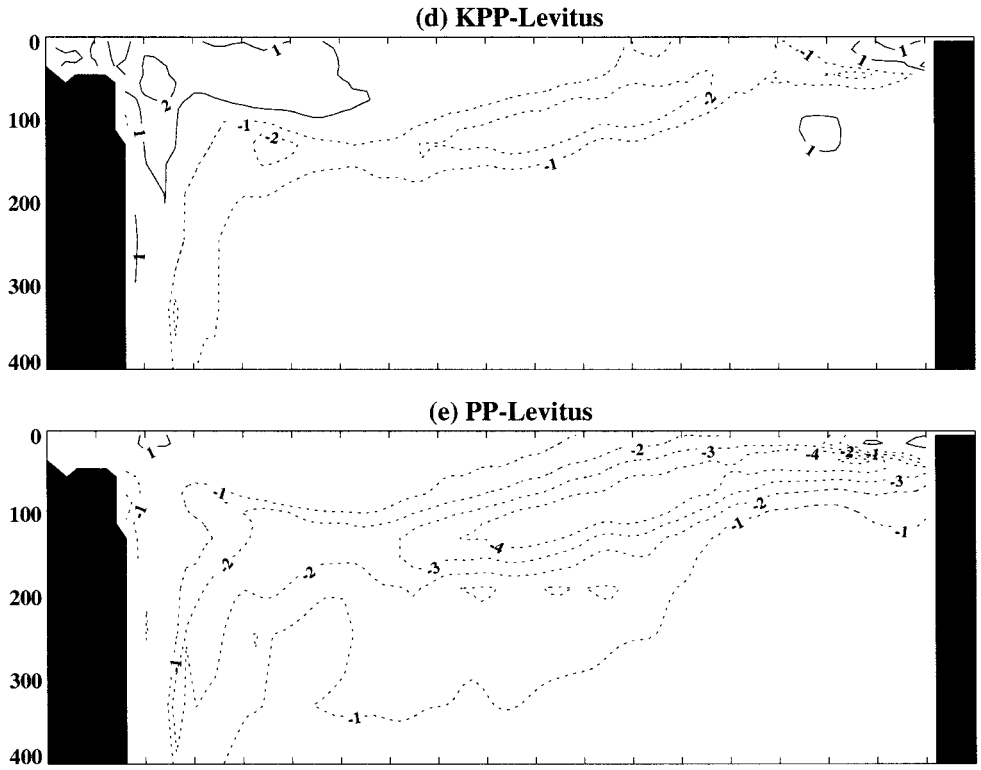

FIG. 3. (*Continued*)

1). Because of the use of the GM parameterization, the horizontal diffusivity is set to zero and a relatively small value of 5×10^5 cm^2 s^{-1} is used for horizontal viscosity, isopycnal diffusivity, and thickness diffusivity. The vertical-mixing terms are treated implicitly. The time step is 1 h.

b. Surface forcing

Surface forcing can be separated into momentum, heat, and freshwater fluxes. The momentum fluxes (τ_u, τ_v) are calculated from the zonal and meridional wind speeds in the Comprehensive Ocean–Atmospheric Data Set (COADS; da Silva et al. 1994) by using the formula based on the Large and Pond (1981) drag formulation. The COADS is selected because it is the longest surface marine dataset covering the whole Pacific basin. The net heat flux Q_t across the ocean surface is given as

$$Q_t = R_S - R_L - Q_S - Q_L, \tag{1}$$

where R_S is the incoming shortwave radiation and R_L is the outgoing longwave radiation. Both R_S and R_L are provided by COADS. The method to compute the solar radiation is the same as described in Rosati and Miyakoda (1998). The sensible heat flux Q_S and the latent heat flux Q_L are calculated through the bulk formula as follows:

$$Q_S = \rho_o C_D C_P |\mathbf{V}|(T - T_A) \tag{2}$$

$$Q_L = \rho_o C_D L |\mathbf{V}|[e_s(T) - \gamma e_s(T_A)](0.622/P_A), \tag{3}$$

where $|\mathbf{V}|$ is the wind speed, T_A is the air temperature (both also derived from COADS), and T is the model-simulated temperature. The impact of spatial variations of sea level pressure is relatively small, and is therefore neglected in the present study. The saturation vapor pressure is

$$e_s(T) = 10^{9.4-2353/T}. \tag{4}$$

The impact of the sea surface salinity on the saturation vapor pressure is much smalled than that of the sea surface temperature, and is therefore neglected in the present study. The constants are $\rho_o = 1.2$ kg m^3, $L = 0.595$ cal kg^{-1}, $C_D = 1.2 \times 10^{-3}$, $C_P = 0.24 \times 10^{-3}$ cal kg^{-1} °C^{-1}, $P_A = 1013$ mb, and the mixing ratio $\gamma = 0.8$. The parameterizations of the kinematic surface fluxes are given by

$$\overline{wu_0} = -\frac{\tau_u}{\rho_0} \tag{5}$$

$$\overline{wv_0} = -\frac{\tau_v}{\rho_0} \tag{6}$$

$$\overline{wt_0} = -\frac{Q_t}{\rho_0 C_{p0}}. \tag{7}$$

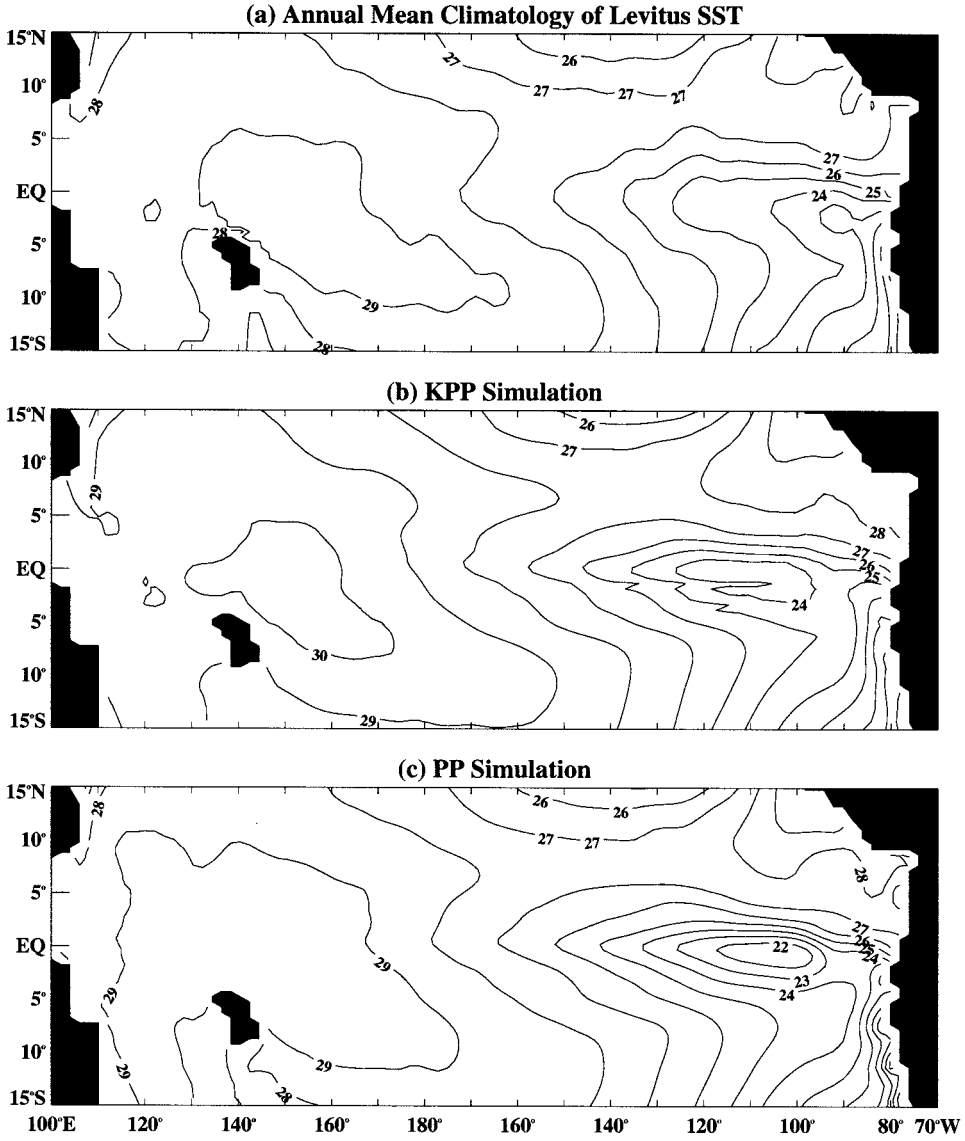

FIG. 4. Annual-mean SST from (a) Levitus climatology, (b) KPP simulation, (c) PP simulation, and the differences between Levitus climatology and (d) KPP and (e) PP simulations. Unit is in °C.

For the model salinity, the climatological freshwater flux, F_t, defined as the precipitation minus evaporation, derived from COADS, is used. In order to compensate uncertainties in the freshwater flux, the model sea surface salinity is also restored toward the value of Levitus monthly mean climatology (Levitus et al. 1994) with a damping timescale of 30 days. The parameterized freshwater flux is

$$\overline{ws_0} = F_t\frac{S_0}{\rho_0} + \gamma_s(S_{\text{Levitus}} - S), \tag{8}$$

where $\gamma_s = dz(1)/30$ days, where $dz(1)$ is the first-level grid depth. The surface buoyancy flux $\overline{wb_0}$ and buoyancy forcing B_f and the buoyancy profile $B(z)$ are calculated as

$$\overline{wb_0} = g(\alpha\overline{wt_0} - \beta\overline{ws_0}) \tag{9}$$

$$B_f = -\overline{wb_0} \tag{10}$$

$$B(z) = g(\alpha T - \beta S), \tag{11}$$

where g is gravitational acceleration, α and β are the thermodynamic expansion coefficients evaluated at local values of T and S, and the subscript 0 specifies the value at the surface.

c. Experiment design

The annual-mean climatological temperature and salinity distributions of Levitus et al. (1994) and Levitus and Boyer (1994) are used for model initial conditions.

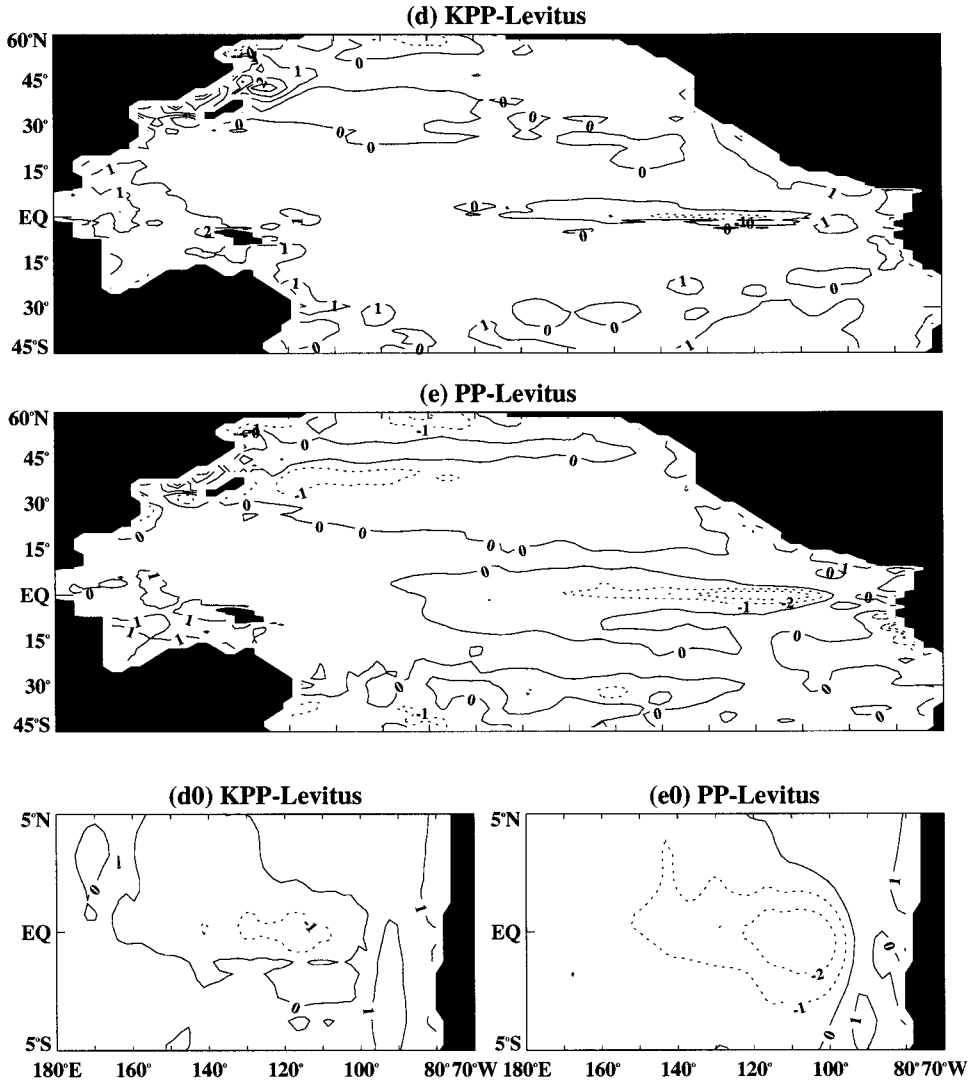

FIG. 4. (*Continued*)

The model ocean was spun up for 30 yr from rest using the COADS monthly mean climatological wind stress, heat, and freshwater fluxes (da Silva et al. 1994). The shortwave radiation is allowed to penetrate below the model ocean surface, leading to subsurface bulk heating using the formula of Paulson and Simpson (1977). For this spinup experiment, as in Barnier et al. (1995), the model heat flux has two components: a prescribed COADS net flux and a correction term proportional to the difference between the COADS climatological SST and the model SST. The correction coefficient is computed based on air–sea variables and is a function of space and time. The COADS monthly mean climatological evaporation and precipitation rates are used to calculate the model freshwater flux. In order to compensate errors in the freshwater flux, the surface salinity is restored toward the Levitus monthly mean climatology with a restoring timescale of 30 days. After 30 yr of model integration, the upper ocean reaches a quasi-equilibrium state. Then, the monthly mean COADS wind stress from January 1945 to December 1993 is used to force the model ocean. Two 49-yr (1945–93) solutions have been obtained. The two simulations differ from each other only by the vertical-mixing schemes: that is, PP versus KPP, which is explained in the following section.

3. The vertical-mixing schemes

a. The Pacanowski and Philander (PP) scheme

With the PP scheme, turbulent mixing in an ocean general circulation model is treated by a first-order local diffusion approach in which the subgrid-scale turbulent vertical kinematic flux of a quantity x (X as the mean) is assumed proportional to the local property gradient

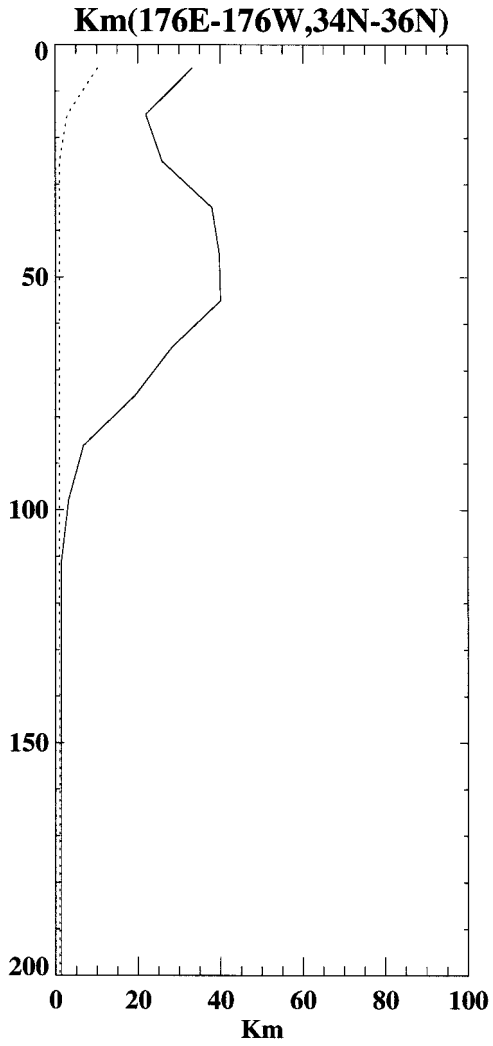

FIG. 5. The mean vertical profile of K_m calculated from Eq. (13) in PP (dotted line) and Eq. (17) in KPP schemes (solid line) in the central North Pacific Ocean region from 176°E to 176°W in long and from 34° to 36°N in lat. Unit is in cm^2 s^{-1}.

with an appropriate eddy mixing coefficient K. This so-called K theory can be described as

$$\overline{wx} = -K\partial_z X, \tag{12}$$

where the upper case (X) represents mean quantities resolved at the model grid and the lower case (x) represents the subgrid-scale variables (also called turbulent fluctuations). The measurements of Crawford and Osborn (1979) and Osborn and Bilodeau (1980) suggest that turbulent mixing processes in the Tropics are strongly influenced by the shear of the mean currents. The mixing coefficients can be approximated as

$$K_m = \frac{\nu_0}{(1 + \alpha \mathrm{Ri}_g)^n} + \nu_b \tag{13}$$

$$K_t = \frac{\nu_0}{(1 + \alpha \mathrm{Ri}_g)^{n+1}} + \kappa_b, \tag{14}$$

where K_m represents viscosity, K_t represents diffusivity, and the local gradient Richardson number

$$\mathrm{Ri}_g = \frac{N^2}{U_z^2 + V_z^2}. \tag{15}$$

As in Pacanowski and Philander (1981), the background viscosity $\nu_b = 1.0$ cm^2 s^{-1}, diffusivity $\kappa_b = 0.1$ cm^2 s^{-1}, $\nu_0 = 100$ cm^2 s^{-1}, $n = 2$, and $\alpha = 5$. Here N represents Brunt–Väisälä frequency and U_z and V_z the vertical shear. In particular, at the model's first level, both K_m and K_t have a minimum value of 10 cm^2 s^{-1} to compensate for the mixing induced by the high-frequency wind fluctuations that are absent from the monthly mean values. For the convection case ($\mathrm{Ri}_g < 0$), a maximum value of 1.0×10^6 cm^2 s^{-1} is used in order to mix the heat instantaneously in the vertical to a depth that ensures a stable density gradient.

b. The K-Profile Parameterization (KPP) scheme

In contrast to the conventional PP scheme, the KPP scheme considers two distinctly nonlocal aspects of large-scale ocean turbulence. The subgrid-scale, turbulent, vertical kinematic flux can be described as

$$\overline{wx} = -K(\partial_z X - \gamma_x), \tag{16}$$

where the term γ_x represents the additional nonlocal transport term besides the familar local downgradient component. The eddy mixing coefficient K everywhere inside the ocean boundary layer (OBL) depends upon both the surface forcing and the depth of the layer as follows:

$$K(\sigma) = hw(\sigma)G(\sigma), \tag{17}$$

where $\sigma = d/h$ represents a dimensionless vertical coordinate, h the OBL depth, d the distance from the surface, $w(\sigma)$ a depth-dependent characteristic velocity called turbulent velocity scale, and $G(\sigma)$ a nondimensional vertical shape function. Equation (16) is applied for temperature, salinity, and other passive tracers. The eddy viscosity, K_m, is also defined as (16) but with w replaced by another velocity scale w_m. With proper formulation of w (or w_m), it can be shown that Eq. (16) behaves well from very stable to very unstable conditions in horizontally homogeneous and quasi-stationary situations (Högström 1988; Large et al. 1994). For unstable conditions, w and w_m are proportional to the so-called convective velocity scale w_*, while for neutral and stable conditions, w and w_m are proportional to the friction velocity u_*. A summary of the velocity scales is given in appendix A.

The depth of the OBL is determined by a bulk Richardson number relative to the surface as

$$\mathrm{Ri}_b = \frac{(B_r - B)d}{(U_r - U)^2 + (V_r - V)^2 + V_t^2}, \tag{18}$$

when $\mathrm{Ri}_b = \mathrm{Ri}_c$ (a critical value of 0.3 used in our

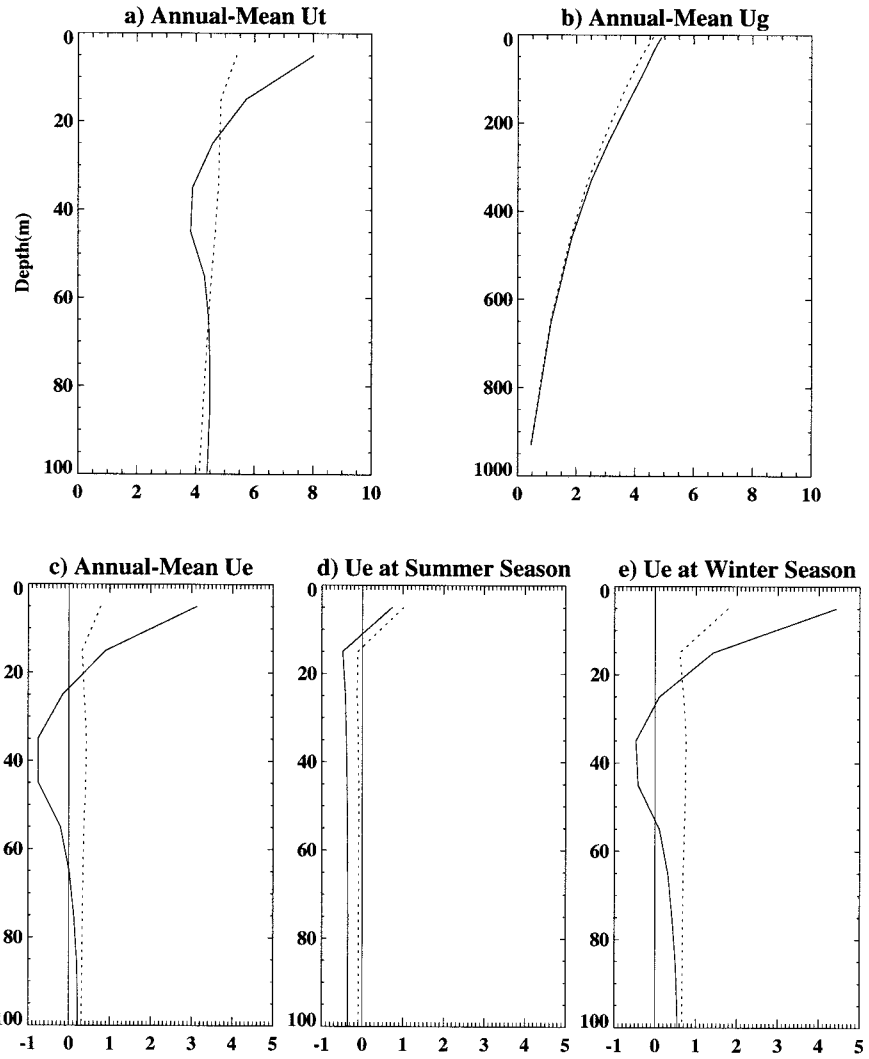

FIG. 6. The vertical profiles of the (a) annual-mean total zonal velocity, (b) the annual-mean geostrophic zonal velocity, (c) the annual-mean zonal Ekman velocity, and (d), (e), two different seasonal mean Ekman velocities averaged in the same region as in Fig. 5. The geostrophic velocity is computed by calculating the geopotential anomalies between 34 and 36°N and is relative to level-19 that is between 768- and 1092-m depth. Unit is in cm s^{-1}. Same as in Fig. 4, PP (dotted) and KPP (solid). Note the different vertical scale in (b).

simulation), the depth is called boundary layer depth *h*. It measures how deep a turbulent boundary layer eddies with a mean velocity (U_r, V_r) and mean buoyancy B_r can penetrate into the interior stratification before becoming stable relative to the local buoyancy and velocity. Both B_r and (U_r, V_r) are estimates of the average buoyancy and velocity, respectively, over the surface thin layer on the top of *h*. In our simulation, since our vertical resolution is rather coarse, they are simply set to the values at the surface first level. The turbulent velocity shear term V_t/d measures the strength of the turbulence and is important in pure convection and other situations of little or no mean shear. Its detailed definition can be found in appendix B. Because of the addition of V_t, *h* can measure the strength of the entrainment from the stratified layer below the surface mixed layer due to the large turbulent eddies.

At all depths inside the OBL, the mixing coefficients are directly proportional to *h*, reflecting the ability of deeper boundary layers to contain larger, more efficient turbulent eddies. The shape function is a cubic polynomial (O'Brien 1970) as

$$G(\sigma) = \sigma(1 + a_2\sigma + a_3\sigma^2). \qquad (19)$$

Obviously, $G(0) = 0$ satisfies the physical condition that turbulent eddies do not cross the surface. The coefficients a_2 and a_3 are computed to make the interior and boundary layer mixing coefficients and their gradients match at $\sigma = 1.0$ ($d = h$). Thus, interior mixing is able to influence the entire boundary layer.

The nonlocal transport term γ_x in Eq. (15) represents the nonlocal impact of the large-scale turbulence mixing and is nonzero only in the boundary layer for tracers under unstable forcing for our present simulations. The detailed description of γ_x can be found in appendix C. Below the boundary layer h, the vertical mixing is parameterized through the local gradient Richardson number and a background mixing coefficient similar as in the PP scheme. Several model sensitivity experiments have been conducted using different KPP parameters. The major results from these sensitivity experiments are summarized in appendix D.

4. Results

In order to distinguish the difference between the KPP and PP simulations, a detailed comparison is made in this section by separating the simulated 49-yr time series into the annual mean state, annual cycle, and interannual-to-interdecadal variability. All the mean states are calculated within the period from 1961 to 1990 unless specifically mentioned otherwise.

a. The mean state

1) TROPICS

The coefficients of vertical eddy viscosity K_m and eddy diffusivity K_t vary considerably in the global oceans. They usually have large values in the surface mixed layer, but have very small values below the thermocline. Figure 1 shows the vertical profile of the mean K_m simulated by both PP (dash) and KPP (solid) schemes at 165°E, 140°W, and 110°W on the equator. As a remarkable difference in the surface of 50–100 m, K_m from the KPP scheme is much larger than K_m from the PP scheme. For the KPP scheme, as observed by Crawford and Osborn (1979), K_m varies from 10 to 100 $\text{cm}^2\ \text{s}^{-1}$ in the top 50-m water column in both the central and eastern equatorial Pacific Ocean. In the western warm pool region, K_m can be even larger, with a value of 250 $\text{cm}^2\ \text{s}^{-1}$ at the surface. As expected, the simulated value of K_m in and below the thermocline is substantially smaller.

Figure 2 shows the vertical distribution of simulated mean zonal velocity on the equator for comparison with the mean Tropical Atmosphere Ocean (TAO) array observation (Yu and McPhaden 1999) at 165°E, 140°W, and 110°W, respectively. Note that the Equatorial Undercurrent (EUC) at 140°W in the KPP solution is much deeper and the depth of the maximum EUC is about 20 m closer to the observation than that in the PP solution. This can be explained as follows: a larger vertical eddy viscosity is parameterized in the KPP scheme and, therefore, more surface kinetic energy can penetrate into the deeper ocean interior across the sharp thermocline through the resolved surface boundary layer. The improvement in the western equatorial Pacific is also evident, even though the Indonesian passages have been closed in the model. At 110°W, the amplitude of the EUC simulated by both schemes is weaker than observations, probably due to the coarse vertical resolution in the thermocline out-cropped region.

In addition to the improvement in simulating the mean tropical current structure, the KPP scheme also produces more realistic thermal structure than the PP scheme. Figure 3 shows the annual-mean temperature along the equator and the differences between the two simulations and the Levitus climatology (Levitus and Boyer 1994). Although both solutions are colder than the Levitus annual-mean climatology, the KPP solution has a stronger vertical temperature gradient than the PP solution, and agrees more with observations. Figure 4 shows the annual-mean SST and the differences between the simulations from both the KPP and PP schemes and the Levitus climatology. When the PP scheme is used, the simulated temperature in the eastern equatorial Pacific Ocean can be more than two degrees colder than the observed (Fig. 4e). This cold bias as described in Stockdale et al. (1993) and Niiler et al. (1995) in the eastern equatorial Pacific is significantly reduced to less than one degree when the KPP scheme is used (Fig. 4d).

2) EXTRATROPICS

In the extratropical region, where shear-dependent mixing is significantly weaker than in the tropical region, the difference can be even more dramatic. This is clearly shown in Fig. 5, where the mean K_m averaged over the central North Pacific region (34°–36°N, 160°E–160°W) is displayed. For the KPP scheme, K_m varies from over 20 to 40 $\text{cm}^2\ \text{s}^{-1}$ inside the surface mixed layer. On the other hand, the PP scheme obviously failed to simulate the vertical eddy viscosity. Similarly, the simulated current structure is different. The mean zonal current and its Ekman component in the central North Pacific Ocean are shown in Fig. 6. The Ekman component from the KPP solution is generally larger than that from the PP solution at the surface (Fig. 6c). The geostrophic velocity relative to that at 1000-m depth is computed from geopotential anomalies between 34° and 36°N. The geopotential anomalies were calculated through the annual-mean distribution of temperature and salinity from the solutions by both schemes. Because the vertical eddy viscosity in the KPP solution is rather larger (Fig. 4b), the Ekman spiral depth

$$D_E = \pi\left(\frac{2K_m}{|f|}\right)^{1/2} \tag{20}$$

is accordingly larger. Based on Fig. 5, an average K_m of about 30 $\text{cm}^2\ \text{s}^{-1}$ can be found for the KPP solution. From Table 2, D_E should be around 27 m. This is consistent with the estimation from the vertical structure of Ekman velocity (Fig. 6c). For the PP solution, K_m is very small except in the first level where a minimum

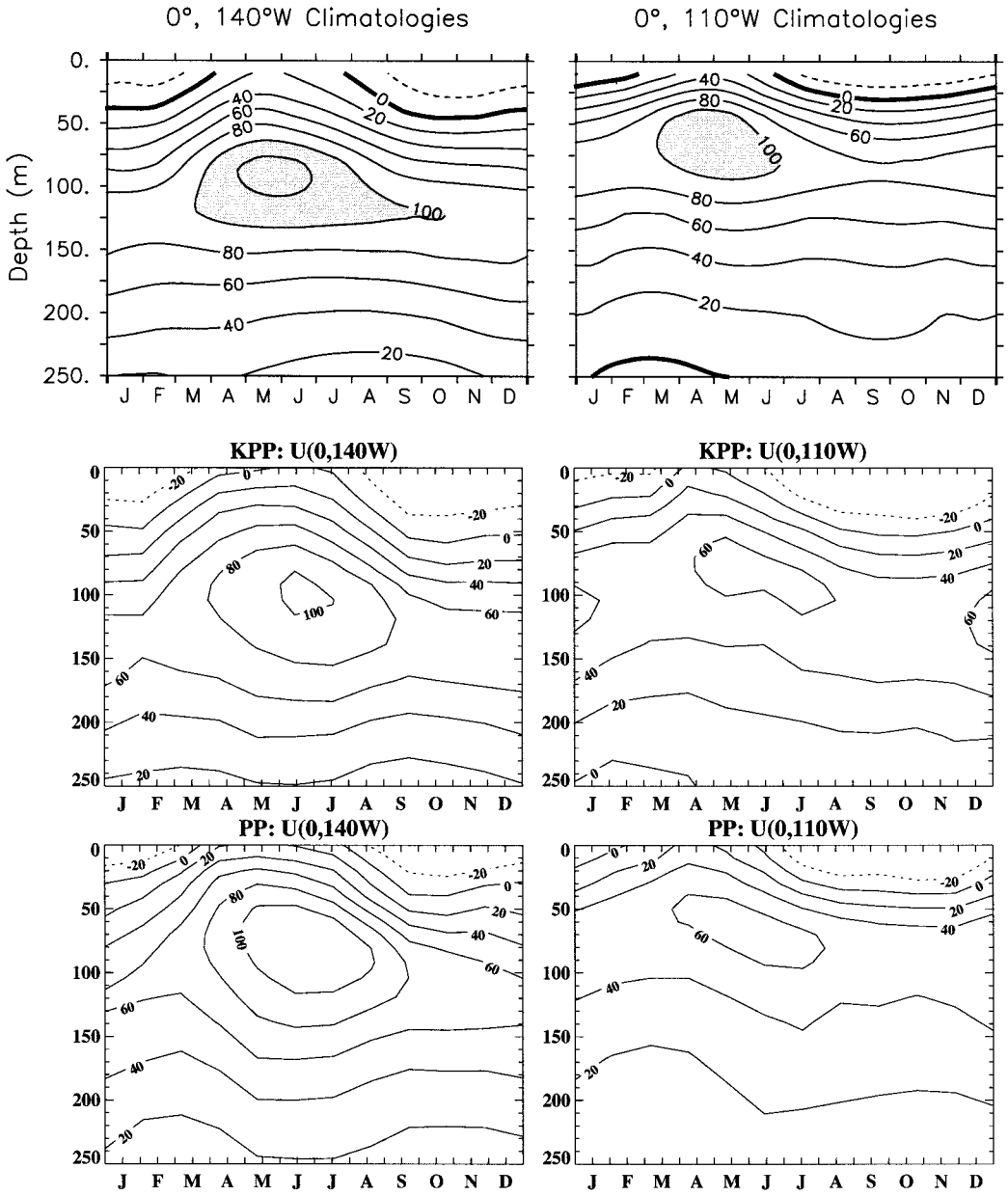

FIG. 7. Annual cycles of equatorial zonal currents from TAO observations taken at upper 140° and 110°W and (middle) from KPP and (lower) PP simulations. TAO observation is from Yu and Schopf (1997). Unit is in cm s^{-1}.

value of 10 cm^2 s^{-1} is specified. Therefore, the Ekman layer from the PP solution is very shallow and almost no evident Ekman layer exists most of the time.

b. The annual cycle

In addition to the mean state, the difference of K_m also results in a different annual cycle of both current and thermal structures.

1) CURRENT

Figure 7 shows the vertical distribution of mean annual cycle of equatorial zonal currents taken at 140° and 110°W during 1980–91 from both observation (Yu and Schopf 1997) and the twin 49-yr (1945–93) simulations. In general, both the phase and amplitude are comparable in both KPP and PP schemes. However, the depth of the maximum current amplitude in spring from the KPP scheme is closer to the TAO observation than the PP scheme. In the extratropical region, the current structure

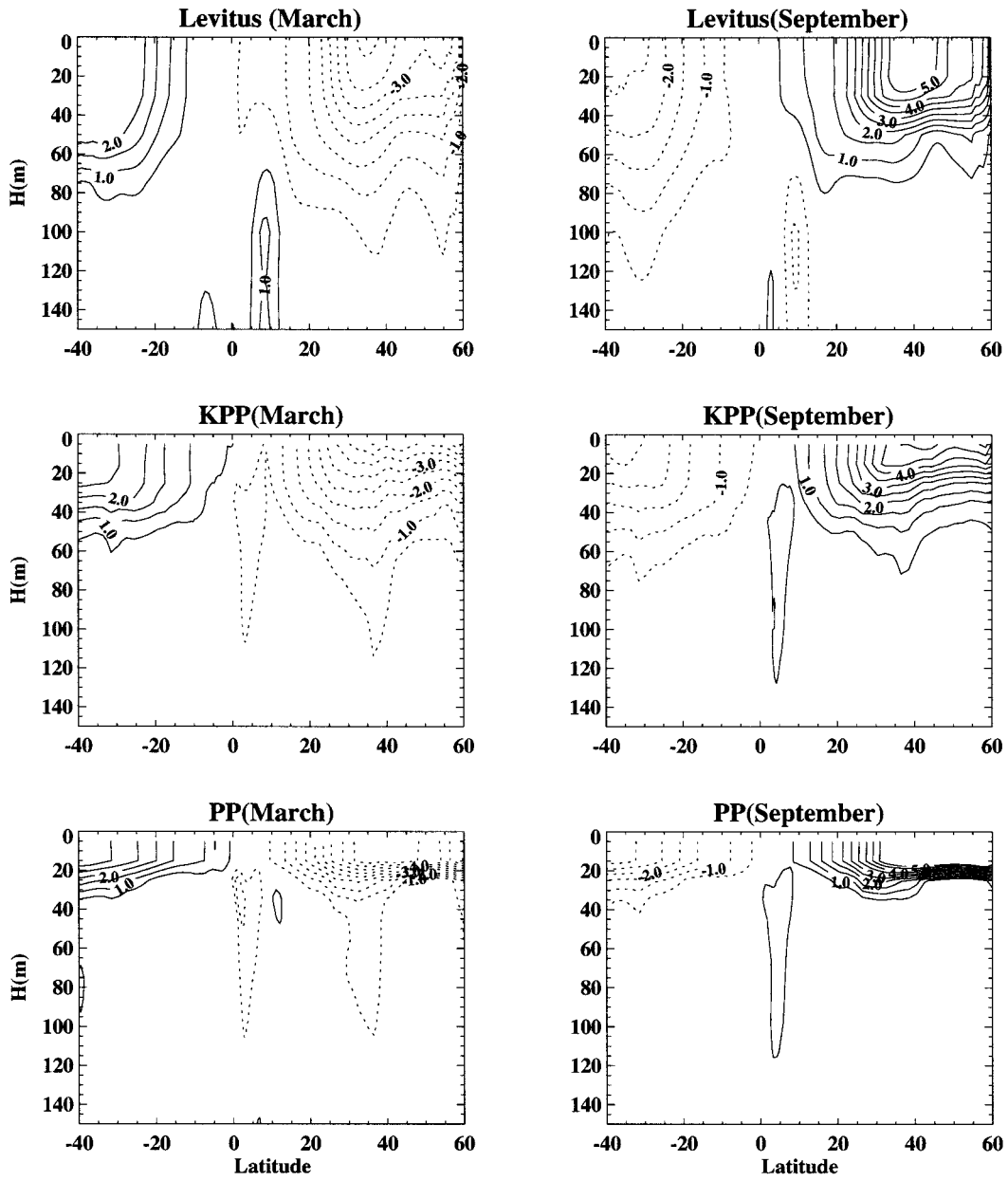

FIG. 8. Zonally averaged temperature anomalies (with annual-mean values removed) (top) as a function of depth and latitude from Levitus climatology, (middle) KPP solution, and (bottom) PP solution for Mar and Sep. Contour interval is 0.5°C.

also exhibits strong seasonal variability as shown in Fig. 6d. In winter (January–March) when the wind is strongest, the zonal component of modeled Ekman Current can reach 4 cm s^{-1}, while it is only about 1 cm s^{-1} in summer (July–September).

2) TEMPERATURE

Figure 8 shows the vertical distribution of zonally averaged mean seasonal temperature anomalies in the whole Pacific basin for March and September. The seasonal temperature anomalies were calculated from the mean seasonal cycle of the last 5 yr of the 30-yr spinup model integration. It can be seen that in the PP solution the mean seasonal temperature anomalies are mostly trapped near the surface. In contrast, in the KPP solution, the mean seasonal temperature anomalies are more realistically distributed in the upper-ocean water column. A layer of 30–50 m deep with a uniform temperature can be found in the subtropics in both hemispheres. The improvement is significant, although it is still shallower in the KPP solution than in the Levitus

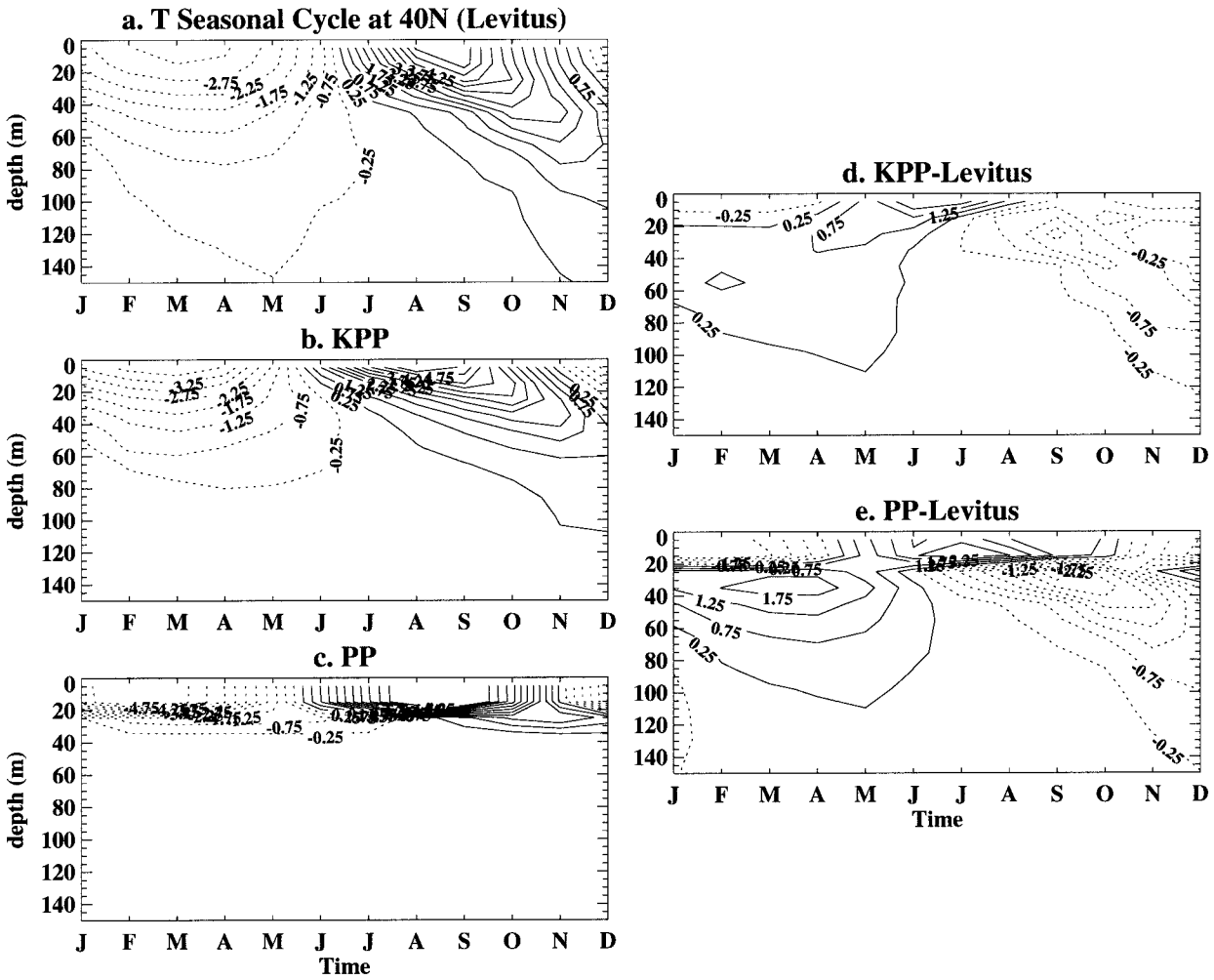

FIG. 9. Zonally averaged temperature anomalies as in Fig. 8 at 40°N as a function of time and depth from (a) Levitus climatology, (b) KPP, and (c) (PP). (d) and (e) The differences between the simulations and Levitus climatology are also shown. Contour interval is 0.5°C.

climatology. It requires more extensive studies to ascertain to what extent the KPP scheme can be further improved, by adjusting the KPP parameters, using alternative surface forcing or interplaying the interaction between the KPP and GM schemes.

Figure 9 shows the zonally averaged mean seasonal temperature anomalies in the midlatitude (40°N) as a function of depth and month from the Levitus climatology and the differences between the two simulations and the Levitus climatology. For the KPP simulation, the difference is less than 1 degree most of the time except for the summer transition period when the monthly variation has the largest value (Fig. 9d). For the PP simulation, the seasonality is overestimated in the thin surface layer (about 20 m) while underestimated in the interior and sandwiched in between with a thin layer of strong gradient, which is obviously unrealistic (Fig. 9e).

Inaccurate simulations of sea surface temperature due to improper mixed layer physics can lead to wrong sensible and latent heat fluxes that will subsequently affect the upper-ocean heat storage. Figure 10 shows the seasonal anomalies of the heat storage (defined as the vertically averaged temperature in the upper 300 m) against the sea surface temperature averaged in the central North Pacific (30°–40°N, 160°E–160°W). It is interesting to note that the KPP solution is significantly better than the PP solution when compared with the Levitus climatology. The PP scheme underestimates the seasonal change of heat storage while overestimating the seasonal change of SST in this midlatitude ocean region, which is consistent with a recent study of Stammer et al. (1996). In particular, the March temperature in the PP solution is 2 degrees colder than the Levitus observation, while the September temperature is over 1 degree warmer. The KPP scheme has resulted in a much larger heat storage capacity in the upper ocean than the PP scheme.

3) BOUNDARY LAYER DEPTH (h)

Based on the turbulence similarity theory, the surface buoyancy and momentum fluxes should be able to pen-

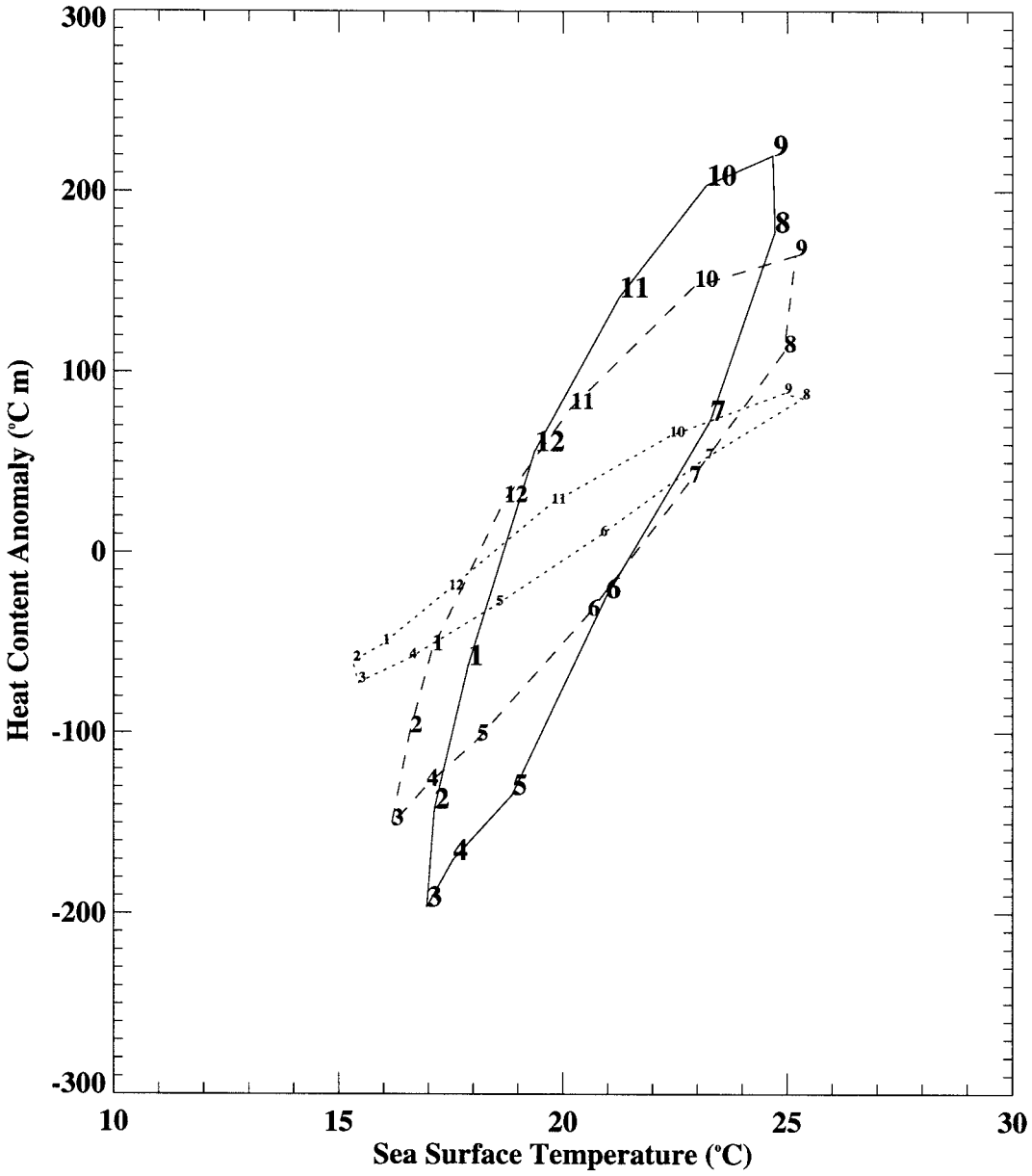

FIG. 10. Heat content anomalies as a function of sea surface temperature from Levitus climatology (solid line), KPP solution (dashed line), and PP solution (dotted line) averaged over a box region from 160°E to 160°W in long and from 25° to 40°N in lat. The heat content anomaly is integrated up to 277 m and averaged over the box region with a unit of °C m. The numbers (1, 2, . . . , 12) represent the months of Jan, Feb, . . . , Dec.

etrate into a depth where they first become stable relative to the local buoyancy and velocity. In the KPP formulation, this boundary layer depth (h) is determined explicitly by calculating the bulk Richardson number relative to the surface according to Eq. (18). Figure 11 shows the monthly mean distribution of h for March. The distribution of h is strongly inhomogeneous, ranging from 10 to more than 100 m. In the central tropical Pacific Ocean, h can change in the range of $30 < h < 100$ m. There is a distinct seasonal cycle for h, mainly due to the seasonal cycle of surface fluxes of buoyancy and momentum. In the Northern Hemisphere spring, h in the Northern Hemisphere is much deeper than that in the Southern Hemisphere. Especially in the Kuroshio Current and its extension region and the central tropical Pacific region, the value of h can be as high as 100 m, implying that the surface momentum and buoyancy fluxes can penetrate as deep as 100 m before they reach stable condition.

For comparison, the distribution of the mixed layer depth (MLD) is also shown in Fig. 11. Following Levitus et al. (1994) and Levitus and Boyer (1994), the

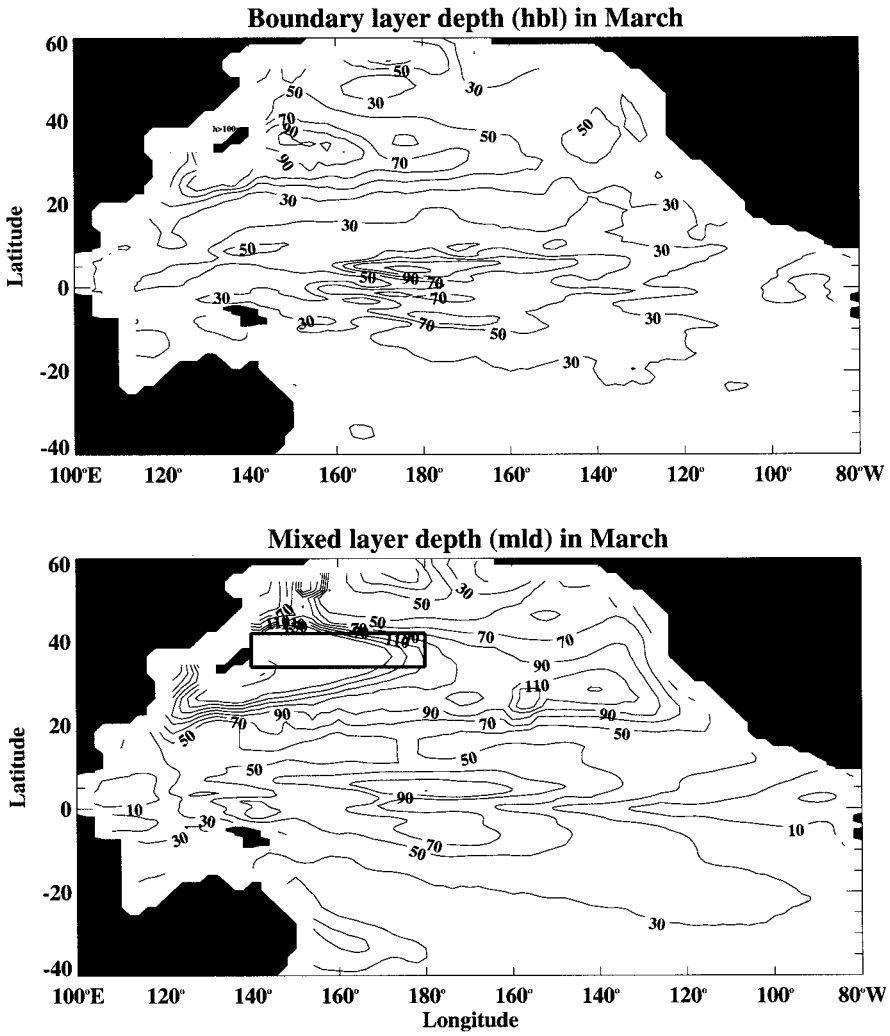

FIG. 11. The distribution of monthly mean boundary layer depth h (above) and monthly mean mixed layer depth (below) from the KPP solution in Mar averaged between 1971 and 1990. Contour interval is 20 m. The mixed layer depth is defined as the depth where σ_t first exceeds its surface value by 0.125 k gm^{-3}. The rectangular box region (below) is defined as the Kuroshio Current Extension (KCE) region used in Fig. 14.

MLD is defined as the depth where the density (σ_t) first exceeds its surface value by 0.125 kg m^{-3}. The MLD depends on the integrated performance of wind and also depends on the stability of the underlying water and on the heat and freshwater balance through the surface. To understand the time-dependent process of mixed layer dynamics is still an active area of research (e.g., Lukas and Lindstrom 1991; Large et al. 1994; Kantha and Clayson 1994). Overall, the distribution pattern of h is similar to that of MLD although MLD is generally deeper than h, mostly due to the Ekman pumping, which is a nonlocal process. This is particularly true in the Kuroshio Current and its extension region and in the central Northeast Pacific region.

The seasonal cycle of h is primarily determined by the seasonal cycle of the surface fluxes, including both wind stirring and radiation fluxes. Figure 12 shows the monthly mean value of the zonally averaged bulk Richardson number around the date line for March and September. The monthly mean values $\overline{h}$ and MLD are also overlaid in Fig. 12. Note that the MLD is much deeper than h especially in the season of winter when the wind stirring is strongest and the turbulent mixing is very intense within the OBL. The distribution of vertical eddy viscosity overlaid by the h and MLD is displayed for March and September in Fig. 13, respectively. Within the OBL, the eddy viscosity K_m defined by Eq. (17) is inhomogeneous in different regions. The vertical distribution is also nonuniform. The values at the bottom of the OBL are larger than those inside of the layer (Fig. 5). Most of them change from $10 < K_m < 100.0$ cm^2 s^{-1} and are seasonally dependent. Below the OBL, K_m

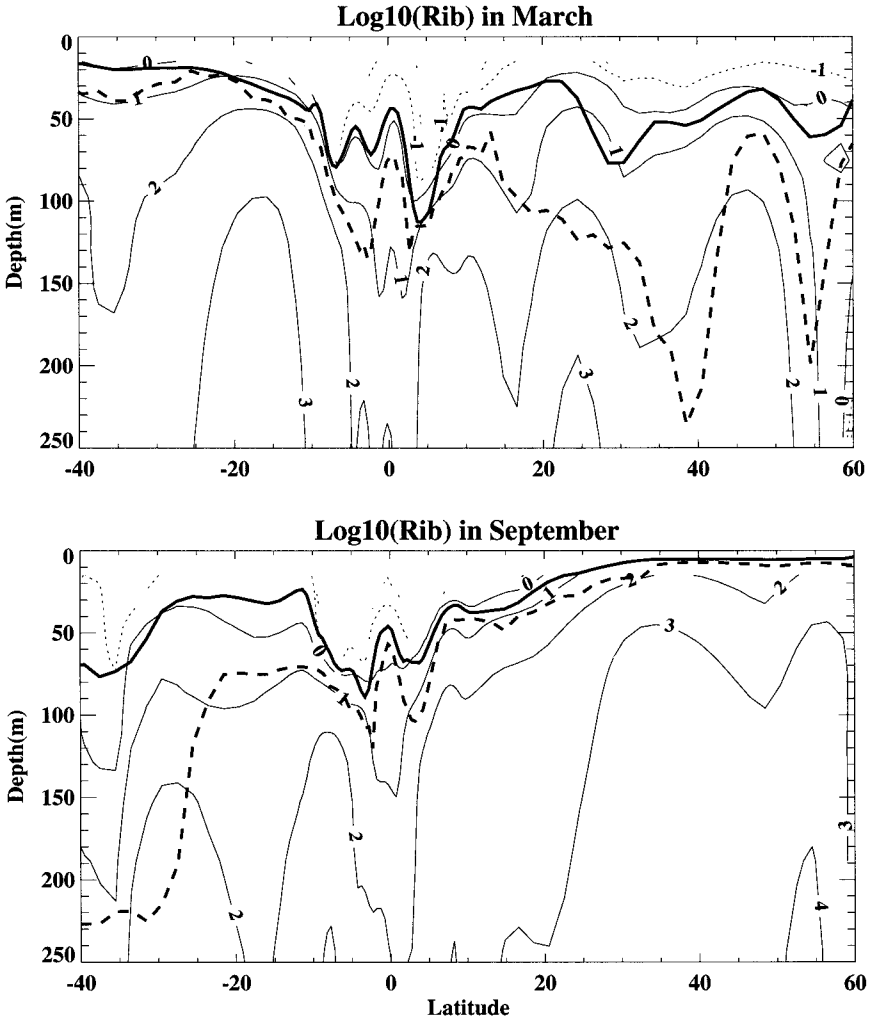

FIG. 12. Monthly mean bulk Richardson number as a function of depth and latitude for Mar and Sep. The bold solid lines represent monthly mean boundary layer depth and the bold dotted lines represent the monthly mean mixed layer depth.

is determined by Eq. (13) and most values are in the range of $1.0 < K_m < 10.0$ cm^2 s^{-1}. The values below the OBL have been matched with those inside the OBL.

c. Interannual-to-interdecadal variability

While the tropical interannual variability associated with ENSO in the Pacific Ocean can be simulated reasonably well by the PP scheme (Philander et al. 1987; Chao and Philander 1993), the extratropical interannual-to-interdecadal variability has not been well simulated with an OGCM (Stammer et al. 1996). A number of recent studies have reported the pronounced interannual-to-interdecadal variability in the extratropical Pacifc Ocean (for recent reviews, see Mantua et al. 1997 and Nakamura et al. 1997). Although the cause of this variability is still a matter of debate, the spatial pattern of the decadal-to-interdecadal variability in the ocean has proven to be strongly three-dimensional by analyzing both SST and subsurface ocean thermal data (Zhang and Levitus 1997). In particular, Deser et al. (1996) presented a detailed analysis of the vertical structure of seasonal thermal anomalies in the upper North Pacific Ocean during 1970–91, emphasizing the role of local interactions between the surface mixed layer and the thermocline in producing subsurface thermal anomalies.

Figure 14 shows the time–depth structures of the seasonal temperature anomalies in the Kuroshio extension region as observed by Deser et al. (1996) and simulated by both the KPP and the PP experiments. Same as Deser et al. (1996), the seasonal temperature anomalies were calculated by removing the monthly mean climatology from 1970 to 1991. The residuals were then averaged seasonally within the Kuroshio extension region (34°–42°N, 140°–180°E). It is interesting to note that the KPP scheme realistically simulates those interannual temperature anomalies with comparable amplitudes and similar phases. As observed, the surface-initiated inter-

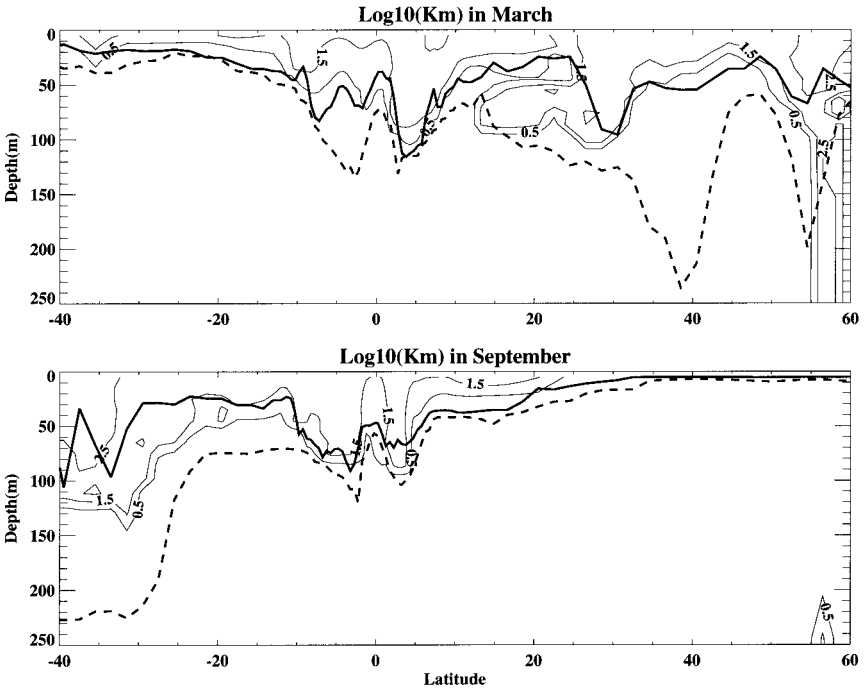

FIG. 13. Monthly mean vertical eddy viscosity calculated from KPP scheme and averaged between 1971 and 1990 as a function of depth and latitude for Mar and Sep at the date line. The bold solid lines represent the monthly mean boundary layer depth and the bold dotted lines represent the monthly mean mixed layer depth.

annual anomalies occurs nearly simultaneously within the upper 400 m and shows very little attenuation with depth. The -0.6°C contour line can reach as deep as 400 m. In contrast, the PP scheme only generates the near-surface interannual anomalies. The vertical penetration of these interannual temperature anomalies simulated by PP is significantly shallower than KPP and observations.

5. Discussions and summary

In this paper we have studied the impact of two different vertical-mixing schemes on the solution of a Pacific OGCM. In the conventional PP scheme, the vertical eddy viscosity and diffusivity are determined based on local vertical gradients of density and velocity. In contrast, the KPP scheme includes nonlocal processes and determines the vertical profiles of eddy viscosity and diffusivity based on a diagnosed boundary layer depth and a turbulent velocity scale. The boundary layer depth is determined through the requirement that surface momentum and buoyancy fluxes should penetrate to a depth where they become stable relative to the local velocity and buoyancy. The turbulent velocity scale is a function of surface wind forcing, buoyancy forcing, and the boundary layer depth. It also incorporates a smooth transition to the parameterization of interior vertical mixing.

The PP and KPP schemes have been compared using two 49-yr (1945–93) simulation experiments forced by monthly mean wind stresses and heat fluxes derived from COADS. The comparison is made in both tropical and extratropical regions for the annual-mean state, annual cycle, and interannual-to-interdecadal variability. Overall, the KPP scheme has produced more realistic simulations of the upper-ocean thermal structures. In the Tropics, the KPP vertical-mixing scheme produces more realistic thermal structures than the PP scheme. For example, the cold bias in the eastern equatorial Pacific has been significantly reduced when KPP is used. In the extratropics, the KPP scheme is significantly better in simulating the temperature anomalies and the upper-ocean heat storage when compared with observations.

Both the mean state and the seasonal cycle of current structures have also been analyzed. It is found that the core of Equatorial Undercurrent in the KPP solution has comparable amplitude but about 20 m deeper than in the PP solution and closer to TAO observations. In the midlatitude, the Ekman spiral depth in the KPP solution is about 20–30 m deep by investigating the current structures in the central North Pacific Ocean region. For the PP solution, the Ekman layer either is too shallow or almost does not exist. The improvement in both the Tropics and the extratropics by KPP can be understood by more realistic vertical profiles of vertical eddy viscosity and diffusivity.

In summary, the KPP scheme works better than the PP scheme in both the Tropics and the extratropics. The PP scheme appears to be applicable only in the Tropics

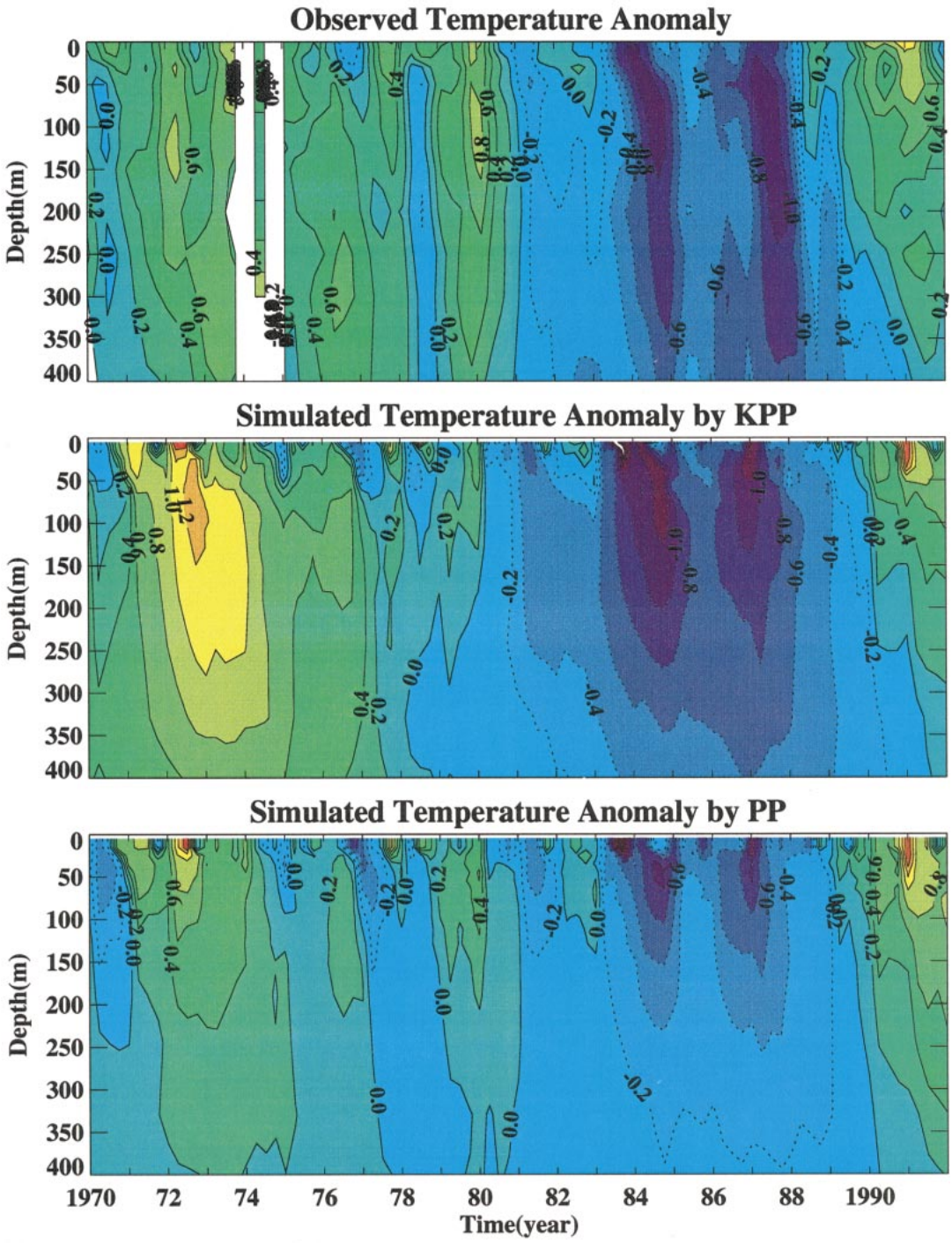

FIG. 14. Monthly mean temperature anomalies as a function of depth and time from (top) Deser et al. (1996), (middle) KPP simulation, and (bottom) PP simulation. The monthly mean temperature anomalies are calculated by averaging the value in the Kuroshio Current Extension (KCE) region (34°–42°N, 140°–180°E, see Fig. 11). Contour interval is 0.2°C. For Deser et al. (1996) observation data, there is a gap in the mid-1970s.

where the shear-dependent instability dominates in the turbulent mixing. In comparison to the high-order turbulence closure schemes, the advantage of the KPP scheme is its relative insensitivity to vertical resolution. Given the correct surface forcing and advective transports, it will properly distribute properties in the vertical according to the empirical functions determined from measurements. From a computational point of view, the

TABLE D1. Sensitivity of zonal velocity amplitude at 140°W on the equator to the critical Richardson number Ri_c in the NCOM climatology run with KPP.

Ri_c	U (cm s^{-1})
0.1	74.0
0.2	77.0
0.3*	84.0
0.4	81.0
0.5	79.0
0.6	80.0

* The value being used in the present study.

TABLE D2. Sensitivity of zonal velocity amplitude at 140°W on the equator to the background ν_b and κ_b in the NCOM climatology run with KPP.

ν_b/κ_b (cm^2 s^{-1})	U (cm s^{-1})
10./0.3	52.0
5./0.2	57.0
3./0.1	58.0
2./0.1	73.0
*1./0.1	84.0
0.1/0.01	83.0

* The value being used in the present study.

addition of the KPP scheme increases only about 10% of the computing time. It is therefore more efficient than high-order turbulence closure schemes, which requires 50% or more computational time (Rosati and Miyakoda 1988).

Although the KPP scheme has made significant improvement in simulating the vertical distrubution of thermal and kinetic energy, there is still room for improvement. It is expected that the KPP solutions can be further improved by adjusting the KPP interior mixing parameters (W. G. Large 1999, personal communication). One of the future studies with the nonlocal KPP scheme should focus on using synoptic forcing (with a high-frequency component, such as diurnal cycle) to drive the ocean boundary layer. In this case, the turbulence will be developed fully inside the boundary layer and the physics of turbulence similarity theory might be more effective in explaining the real situation. The sensitivity of the KPP scheme to salinity and freshwater flux and its potential impact on simulating the low-frequency thermal variability also require further investigation.

Acknowledgments. The research described in this paper was carried out, in part, by the Jet Propulsion Laboratory (JPL), California Institute of Technology, under contract with National Aeronautics and Space Administration. Support from the JPL Director's Research and Development Fund is acknowledged. We'd like to thank Dr. Clara Deser and Michael S. Timlin for providing us the XBTs data used in Fig. 14, the TAO project office and Margie McCarty at NOAA PMEL for providing the observed current data used in Fig. 7, and Arlindo M. da Silva at Goddard Space Flight Center for providing the COADS data. Computations were performed on the Cray J90 through the JPL Supercomputing Project.

APPENDIX A

The Turbulent Velocity Scales in the Nonlocal KPP Scheme

The turbulent velocity scale of Eq. (17) depends primarily on the relative height d/h (h is the OBL depth) and the stability within the OBL (Högström 1988; Holtslag and Boville 1993; Large et al. 1994). Here, stability is defined with respect to the surface active heat flux $\overline{wt_o}$, or equivalently with the ratio h/L (L being the Monin–Obukhov length scale). Secondly, the velocity scales are also dependent on the specific quantity of interest. We will assume that the velocity scales for mixing of scalars, such as temperature and salinity, are equally denoted by w_t. For the momentum component, the velocity scale is different and denoted by w_m. The specification of w_t and w_m is given in details by Large et al. (1994).

For stable ($\overline{wt_0} < 0$ or $h/L > 0$) and neutral surface conditions ($\overline{wt_0} = 0$ or $h/L = 0$), the velocity scale for passive tracer is

$$w_t = \frac{u_*}{\phi_t}, \tag{A1}$$

where u_* is the friction velocity defined by

$$u_*^2 = (\overline{wu_0}^2 + \overline{wv_0}^2)^{1/2}. \tag{A2}$$

Meanwhile ϕ_t is the dimensionless vertical temperature gradient given by

$$\phi_t = 1 + 5\frac{d}{L}, \quad \text{for } \frac{d}{L} \geq 0. \tag{A3}$$

Here L is the Monin–Obukhov length and is defined by

$$L = \frac{-u_*^3}{k(\alpha g)\overline{wt_0}}, \tag{A4}$$

where $k = 0.4$ is called von Kármán's constant, α is thermodynamic expansion coefficient, g is the gravitational acceleration. In stable conditions, the exchange coefficients for heat and momentum are often found to be similar (Large et al. 1994). Therefore, we use in the model $w_m = w_t$.

For unstable conditions ($\overline{wt_0} > 0$ or $h/L < 0$), the forms w_t and w_m differ from each other and the difference could be dramatic for strong convective situation. In general, for unstable profile, the OBL can be treated as two layers: thin surface layer and deeper boundary layer. For the thin surface layer (usually $d/L \geq -1.0$ for heat), w_t is given by Eq. (A1) and

$$\phi_t = (1 - 16d/L)^{-1/2}. \tag{A5}$$

Similarly w_m is written as

$$w_m = \frac{u_*}{\phi_m} \qquad \left(\frac{d}{L} \le 1.0\right), \tag{A6}$$

where ϕ_m is the dimensionless current speed gradient given by

$$\phi_m = (1 - 16d/L)^{-1/4} \qquad (d/L \le -0.2). \tag{A7}$$

For the deeper layer, ϕ_t and ϕ_m can be written as

$$\phi_t = (-28.86 - 98.96d/L)^{-1/3} \qquad (d/L \le -1.0), \tag{A8}$$

$$\phi_m = (1.26 - 8.38d/L)^{-1/3} \qquad (d/L \le -0.2). \tag{A9}$$

All these unstable forms match the stable functions at $d/L = 0$ (neutral state) and are based upon the available data (Högström 1988). As you can see from Large et al. (1994, Fig. B1), for all $d/L < 0$, $\phi_m > \phi_t$, therefore, $w_m < w_t$, convection always mixes scalar tracers, including buoyancy, more efficiently than momentum.

For the pure convective situation when u_* approaches zero, the ocean boundary layer turbulence is well behaved because it becomes dependent on a convective velocity scale defined by

$$w_* = (-B_f h)^{1/3}. \tag{A10}$$

Combining all these equations leads to

$$w_x = k(a_x u_*^3 + c_x k\sigma w_*^3)^{1/3}. \tag{A11}$$

For the convective limit, the relation becomes as

$$w_x = k(c_x k\sigma)^{1/3} w_*. \tag{A12}$$

APPENDIX B

Turbulent Velocity Shear

The destabilizing shear term of Eq. (18), besides having the magnitude squared of the vector mean velocity difference from (U_r, V_r), also includes another term $V_t(d)$, called turbulent velocity shear (strictly speaking, equal to V_t/d), which is often not negligible and is most important in pure convection and other situations of little or no mean shear. Therefore this term needs to be parameterized. First of all, it should increase with the turbulent velocity scale and decrease with stratification $\partial_z B = N^2$, where N is the local buoyancy frequency. These dependencies and dimensional considerations suggest that

$$\left(\frac{V_t}{d}\right)^2 \propto \frac{Nw_x}{d}. \tag{B1}$$

In order to determine the detailed form of V_t, a special case of pure convection ($u_* = 0$, $B_f < 0$) and no mean shear with a well-mixed layer of buoyancy B_r eroding into a layer of constant stratification, N, is considered. As an empirical rule of convection, the ratio of entrainment flux $\overline{wb_e}$ and surface buoyancy flux $\overline{wb_o}$ in this case $\overline{wb_e}/\overline{wb_o} = \beta_T$ (Fig. 1 at Large et al. 1994). The convection rule, plus relations Eqs. (16), (17), and the assumption of $\gamma_b \ll N^2$. Notice that the numerator of Eq. (18) at $d = h$ becomes $h(h - h_e)N^2$. So we have $G(h_e/h) = [(h - h_e)^2]/h^2$ and $N(h_e) = N/C_v$, constant $1 < C_v < 2$ ($C_v = 1.6$ in our simulation that accounts for some smoothing of buoyancy profile at h_e caused by mixing).

Eliminating h_e, we can get

$$V_t^2(h) = \frac{C_v(-\beta_T)^{1/2}}{\mathrm{Ri}_c k^{2/3}}(c_s\varepsilon)^{-1/6} hNw_*. \tag{B2}$$

Using the scalar (A12) to go from the pure convective to the general case gives

$$V_t^2(d) = \frac{C_v(-\beta_T)^{1/2}}{\mathrm{Ri}_c k^2}(c_s\varepsilon)^{-1/2} dNw_t. \tag{B3}$$

Without the V_t^2 term in Eq. (18), cases of larger N at the bottom of the boundary layer would tend to have smaller entrainment fluxes because the larger buoyancy gradient is insufficient to compensate for the very much smaller diffusivity resulting from the smaller h. However, with this term the larger N gives a larger h from Eq. (18), and hence for a fixed h_e the smaller h_e/h and the larger h increase the diffusivity in Eq. (17) just enough to keep the entrainment flux independent of N. Although the ratio of this flux to the surface buoyancy flux will be a constant $-\beta_T$ in the convective limit, it will depend on u_* in forced convection.

APPENDIX C

Nonlocal Transport Term γ_x

The nonlocal transport term in Eq. (16), γ_x, which represents nonlocal impact of the large-scale turbulence mixing, is nonzero only for scalar tracers under unstable forcing. In such cases, as was suggested by Large et al. (1994), it has been successfully parameterized by Mailbôt and Benoit (1982) as

$$\gamma_x = C\frac{\overline{wx_o}}{w_* h}, \tag{C1}$$

where $w_* = (-B_f h)^{1/3}$ is called convective velocity scale, $C = 10$, a constant in a highly convective situation. This nonlocal transport represents those important processes of turbulent mixing in the boundary layer where there are various coherent structures, such as buoyant vertical plumes, Langmuir circulation, Kelvin–Helmholtz waves, and internal gravity waves. The significance of this nonlocal transport term in different situations remains to be determined.

APPENDIX D

Model Sensitivity Experiments to KPP Parameters

Before conducting our 45-yr OGCM simulation, we have conducted several sensitivity experiments forced

with climatological air–sea fluxes with regard to various KPP parameters. We have compared our simulated annual-mean zonal current amplitude at 140°W on the equator against the observed value from TAO observations (100 $cm^2\ s^{-1}$).

Table D1 shows the sensitivity of model-simulated EUC amplitude with various values of critical Richardson number (Ri_c) used in the KPP formulation. The boundary layer depth (h) is determined at a depth where the bulk Richardson number (Ri_b), as defined in the Eq. (18), equals to the critical Richardson number (Ri_c). Based on these sensitivity experiments, we have selected a critical Richardson number of 0.3 in the present study that yields the best agreement with the available observations.

Table D2 shows the model sensitivity to the background viscosity ν_b and diffusivity κ_b used in Eqs. (13) and (14), respectively. Clearly, the amplitude of the EUC is sensitive to the background viscosity and diffusivity being used. The original NCOM formulation, with the background viscosity and diffusivity of 10.0 and 0.3, significantly underestimated the amplitude of the EUC. It is interesting to note that there is very little sensitivity when the background viscosity/diffusivity goes below 1.0/0.1, which is the value used in our final calculation.

REFERENCES

Ayotte, K. W., and Coauthors, 1996: An evaluation of neutral and convective planetary boundary-layer parameterizations relative to large eddy simulations. *Bound.-Layer Meteor.,* **79,** 131–175.

Barnier, B., L. Siefridt, and P. Marchesiello, 1995: Thermal forcing for a global ocean circulation model using a 3-year climatology of ECMWF analysis. *J. Mar. Sci.,* **6,** 363–380.

Blanke, B., and P. Delecluse, 1993: Variability of the tropical Atlantic Ocean simulated by a general circulation model with two different mixed-layer physics. *J. Phys. Oceanogr.,* **23,** 1363–1388.

Bryan, K., 1969: A numerical method for the study of the world ocean. *J. Comput. Phys.,* **4,** 347–376.

——, and L. J. Lewis, 1979: A water mass model of the world ocean. *J. Geophys. Res.,* **84,** 2503–2514.

Chao, Y., and S. G. H. Philander, 1993: On the structure of the Southern Oscillation. *J. Climate,* **6,** 450–469.

Chen, D., L. M. Rothstein, and A. J. Busalacchi, 1994: A hybrid vertical mixing scheme and its application to tropical ocean models. *J. Phys. Oceanogr.,* **24,** 2157–2179.

Cox, M. D., 1984: A primitive equation, 3-dimensional model of the ocean. GFDL Ocean Group Tech. Rep. 1, 143 pp. [Available from GFDL, P.O. Box 308, Princeton, NJ 08542.]

Crawford, W. R., and T. R. Osborn, 1979: Microstructure measurements in the Atlantic Equatorial Undercurrent during GATE. *Deep-Sea Res.,* **26** (Suppl. II), 285–308.

da Silva, A. M., C. C. Young, and S. Levitus, 1994: *Atlas of Surface Marine Data 1994.* Vol. 1, *NOAA Atlas NESDIS,* 83 pp.

Deser, C., M. A. Alexander, and M. S. Timlin, 1996: Upper ocean thermal variations in the North Pacific during 1970–1991. *J. Climate,* **9,** 1840–1855.

Garwood, R. W., 1977: An oceanic mixed layer model capable of simulating cyclic states. *J. Phys. Oceanogr.,* **7,** 455–467.

Gent, P. R., and J. C. McWilliams, 1990: Isopycnal mixing in ocean circulation models. *J. Phys. Oceanogr.,* **20,** 150–155.

——, F. O. Bryan, G. Danabasoglu, S. C. Doney, W. R. Holland, W. G. Large, and J. C. McWilliams, 1998: The NCAR Climate System Model global ocean component. *J. Climate,* **11,** 1287–1306.

Gnanadesikan, A., and R. A. Weller, 1995: Structure and instability of the Ekman spiral in the presence of surface gravity waves. *J. Phys. Oceanogr.,* **25,** 3148–3171.

Haidvogel, D. B., and A. Beckmann, 1999: *Numerical Ocean Circulation Modeling.* Imperial College Press, 318 pp.

Halpern, D., Y. Chao, C. C. Ma, and C. R. Mechoso, 1995: Comparison of tropical Pacific temperature and current simulations with two vertical mixing schemes embedded in an ocean general circulation model and reference to observations. *J. Geophys. Res.,* **100,** 2515–2523.

Högström, U., 1988: Non-dimensional wind and temperature profiles in the atmospheric surface layer: A re-evaluation. *Bound.-Layer Meteor.,* **42,** 55–78.

Holtslag, A. A., and B. A. Boville, 1993: Local versus nonlocal boundary-layer diffusion in a global climate model. *J. Climate,* **6,** 1825–1842.

Kantha, L. H., and C. A. Clayson, 1994: An improved mixed layer model for geophysical applications. *J. Geophys. Res.,* **99** (C12), 25 235–25 266.

Kraus, E. B., and J. S. Turner, 1967: A one-dimensional model of the seasonal thermocline. II: The general theory and its consequences. *Tellus,* **19,** 98–105.

Large, W. G., and S. Pond, 1981: Open ocean momentum flux measurements in moderate to strong winds. *J. Phys. Oceanogr.,* **11,** 324–336.

——, and P. R. Gent, 1999: Validation of vertical mixing in an equatorial ocean model using large eddy simulations and observations. *J. Phys. Oceanogr.,* **29,** 449–464.

——, J. C. McWilliams, and S. C. Doney, 1994: Oceanic vertical mixing: A review and a model with a nonlocal boundary layer parameterization. *Rev. Geophys.,* **32,** 363–403.

——, G. Danabasoglu, S. C. Doney, and J. C. McWilliams, 1997: Sensitivity to surface forcing and boundary layer mixing in a global ocean model: Annual-mean climatology. *J. Phys. Oceanogr.,* **27,** 2418–2447.

Levitus, S., and T. P. Boyer, 1994: *Temperature.* Vol. 4, *World Ocean Atlas 1994, NOAA Atlas NESDIS,* 117 pp.

——, R. Burgett, and T. P. Boyer, 1994: *Salinity.* Vol. 3, *World Ocean Atlas 1994, NOAA Atlas NESDIS,* 99 pp.

Lukas, R., and E. Lindstrom, 1991: The mixed layer of the western equatorial Pacific Ocean. *J. Geophys. Res.,* **96** (Suppl.), 3343–3357.

Mailhôt, J., and R. Benoit, 1982: A finite-element model of the atmospheric boundary layer suitable for use with numerical weather prediction models. *J. Atmos. Sci.,* **39,** 2249–2266.

Mantua, J. N., S. R. Hare, Y. Zhang, J. M. Wallace, and R. C. Francis, 1997: A Pacific interdecadal climate oscillation with impacts on salmon production. *Bull. Amer. Meteor. Soc.,* **78,** 1069–1080.

McWilliams, J. C., P. P. Sullivan, and C. H. Moeng, 1997: Langmiur turbulence in the ocean. *J. Fluid Mech.,* **334,** 1–30.

Mellor, G. L., and T. Yamada, 1982: Development of a turbulence closure model for geophysical fluid problems. *Rev. Geophys.,* **20,** 851–872.

Nakamura, H., G. Lin, and T. Yamagata, 1997: Decadal climate variability in the North Pacific during recent decades. *Bull. Amer. Meteor. Soc.,* **78,** 2215–2225.

Niiler, P. P., and Coauthors, 1995: Comparison of TOGA tropical Pacific Ocean model simulations with the WOCE/TOGA surface velocity programme drifter data set. World Climate Research Programme Rep. WCRP-1995, 156 pp. [Available from Pearn Niiler, Scripps Institution of Oceanography, University of California, San Diego, La Jolla, CA 92093.]

O'Brien, J. J., 1970: A note on the vertical structure of the eddy exchange coefficient in the planetary boundary layer. *J. Atmos. Sci.,* **27,** 1213–1215.

Osborn, T. R., and L. E. Bilodeau, 1980: Temperature microstructure in the equatorial Atlantic. *J. Phys. Oceanogr.,* **10,** 66–82.

Pacanowski, R., and S. G. H. Philander, 1981: Parameterization of

vertical mixing in numerical models of tropical oceans. *J. Phys. Oceanogr.*, **11,** 1443–1451.

——, K. Dixon, and A. Rosati, 1991: The GFDL modular ocean model user guide. GFDL Ocean Group Tech. Rep. 2, Geophysical Fluid Dynamics Laboratory, Princeton, NJ, 16 pp. [Available from GFDL, P.O. Box 308, Princeton, NJ 08542.]

Paulson, C. A., and J. J. Simpson, 1977: Irradiance measurements in the upper ocean. *J. Phys. Oceanogr.*, **7,** 952–967.

Peters, H., M. C. Gregg, and J. M. Toole, 1988: On the parameterization of equatorial turbulence. *J. Geophys. Res.*, **93,** 1199–1211.

Philander, S. G. H., W. Hurlin, and A. D. Seigel, 1987: A model of the seasonal cycle in the tropical Pacific Ocean. *J. Phys. Oceanogr.*, **17,** 1986–2002.

Price, J. F., R. A. Weller, and R. Pinkel, 1986: Diurnal cycling: Observations and models of the upper ocean response to diurnal heating, cooling and wind mixing. *J. Geophys. Res.*, **91,** 8411–8427.

Robinson, A. R., 1966: An investigation into the wind as the cause of the Equatorial Undercurrent. *J. Mar. Res.*, **24,** 179–191.

Rosati, A., and K. Miyakoda, 1988: A general circulation model for upper ocean simulation. *J. Phys. Oceanogr.*, **18,** 1601–1622.

Sarmiento, J. L., and K. Bryan, 1982: An ocean transport model for the North Atlantic. *J. Geophys. Res.*, **87,** 394–403.

Stammer, D., R. Tokmakian, A. Semtner, and C. Wunsch, 1996: How well does a 1/4 global circulation model simulate large-scale oceanic observations? *J. Geophys. Res.*, **101,** 25 779–25 801.

Stockdale, T., D. Anderson, M. Davey, P. Delecluse, A. Kattenberg, Y. Kitamura, M. Latif, and T. Yamagata, 1993: Intercomparison of tropical ocean GCMS. Report WCRP-79, WMO/TD 545, World Meteorological Organization, 18–21.

Yu, X., and M. J. McPhaden, 1999: Seasonal variability in the equatorial Pacific. *J. Phys. Oceanogr.*, **29,** 925–947.

Yu, Z., and P. S. Schopf, 1997: Vertical eddy mixing in the tropical upper ocean: Its influence on zonal currents. *J. Phys. Oceanogr.*, **27,** 1447–1458.

Zhang, R.-H., and S. Levitus, 1997: Structure and cycle of decadal variability of upper ocean temperature in the North Pacific. *J. Climate*, **10,** 710–727.